ORIGINAL RESEARCH ARTICLE

Experimental and Numerical Investigation of a Solidification-Based Aluminum-Cooled Finger Refinement Process From Micro to Macro-Scale

DANILO CURTOLO, CHRISTIAN SCHUBERT, ALEXANDRE VIARDIN, SEMIRAMIS FRIEDRICH, MORITZ EICKHOFF, BERND BÖTTGER, BERND FRIEDRICH, HERBERT PFEIFER, and MARKUS APEL

The interest in ultra-pure metals is steadily growing due to the increasing demand for these materials in modern technology. To be able to meet the increasing demand in the future, it is necessary to implement more efficient and productive processes. As a fractional crystallization method in this application area, the cooled finger method exhibits higher productivity and lower energy requirements when compared to industry well-established methods like zone melting. In this study, the mechanisms and relevant phenomena crucial for a successful implementation of a cooled finger process were investigated using a multidisciplinary approach. With carefully selected process parameters, we present here an experimental setup with a purification potential of approximately 80 pct. Additional micro- and macro-scale simulations demonstrate that the process is sensitive to parameters such as rotation rate, cooling rate, and temperature gradient within the melt, which explains the difficulty in optimizing this process in practice. An analysis and description of various phenomena that characterize the behavior of the cooled finger process are presented within this multi-scale approach. As a result, these approaches can also be transferred to the description of processes for other metals, opening application areas outside of the purification of aluminum.

https://doi.org/10.1007/s11661-023-07147-0

I. INTRODUCTION

ALUMINUM in its primary form—from Hall–Héroult process—has a purity range of 2N7 to 3N.[1] While such purity is normally sufficient for the majority of industrial applications and alloying, the need for higher purity levels grows together with the advances of modern technology. Fields such as semiconductor, electronics, automotive, aerospace, high precision instruments, batteries, and superconducting are some examples of high-purity and ultra-high-purity applications of aluminum.[2]

The high-volume and industrial production of ultra-pure aluminum follows two main routes: three-layer electrolysis and fractional crystallization. Both processes can be performed separately to achieve purities of up to 4N8 or in series for higher purification levels reaching 7N.[3,4] Other alternative routes such as vacuum distillation are reported in the literature and can be used for low volume production and/or highly specialized applications.[5]

A. *Fractional Crystallization of Aluminum*

The production of ultra-pure aluminum *via* fractional crystallization (a.k.a. segregation) has been since many decades performed as an alternative to the cost- and investment-intensive three-layer electrolysis. The fractional crystallization mechanism promotes the expelling of the impurities from the crystallization interface. In fractional crystallization, the difference between the solubility of the impurity elements in both solid and liquid phases of the base metal is explored to crystallize a solid with lower impurities content than the initial molten phase.[6,7] The ratio between the concentration of an impurity element in the solid (C_S) and the liquid (C_L) phase is called distribution coefficient (k). This

DANILO CURTOLO, SEMIRAMIS FRIEDRICH, and BERND FRIEDRICH are with the IME - Institute of Process Metallurgy and Metal Recycling, RWTH Aachen University, Intzestraße 3, 52072 Aachen, Germany. Contact e-mail: dcurtolo@ime-aachen.de CHRISTIAN SCHUBERT, MORITZ EICKHOFF, and HERBERT PFEIFER are with the IOB - Department for Industrial Furnaces and Heat Engineering, RWTH Aachen University, Kopernikusstraße 10, 52074 Aachen, Germany. ALEXANDRE VIARDIN, BERND BÖTTGER, and MARKUS APEL are with the ACCESS e.V., Intzestraße 5, 52072 Aachen, Germany.
Manuscript submitted March 1, 2023; accepted July 18, 2023.

Published online: 03 August 2023

coefficient indicates the maximum theoretical impurity segregation that can be achieved in one step of purification.[8] In Table I, the literature values of the k coefficient of most impurities present in aluminum are compiled.[4,9–12]

The values of C_S and C_L can be easily taken from a binary phase diagram of any element dissolved in the metal. The value of k can vary from less than 10^{-3} to greater than 10. Impurities that have a k value lower than unity consist of the majority of impurities present in metals and can be segregated to the liquid phase during crystallization.[6,13] On the other hand, impurities with k higher than unity tend to be incorporated into the forming solid during crystallization. For Al, the elements V, Ti, Cr, and Zr belong to this category, and can be removed prior crystallization with the stoichiometric addition of boron to form non-soluble borides. Any eventual excess of B $k < 1$ will be removed during the crystallization. Some impurities like Pb, Bi, Cd, present themselves with a monotectic crystallization behavior, *i.e.*, the formation of a solid phase and a secondary liquid phase upon crystallization. For these cases, two stages of crystallization can occur depending on whether the impurity concentration is higher than its solid solubility in the metal matrix. For concentrations lower than the solid solubility, the impurity behaves as any other impurity with $k < 1$ with no secondary liquid phase formed.[13]

Table I. Literature Values of Distribution Coefficients of Impurities in Aluminum[4,9–12]

Elements	Distribution Coefficient k	Elements	Distribution Coefficient k
Fe	0.018 to 0.053	Ti	7 to 11
Cu	0.15 to 0.153	Si	0.082 to 0.12
Ag	0.2 to 0.3	K	0.56
Au	0.18	Zr	2.3 to 3
Zn	0.35 to 0.47	Pb	0.0007 to 0.093
Ni	0.004 to 0.09	P	< 0.01
Mn	0.55 to 0.9	Sc	0.9
Mg	0.29 to 0.5	Sb	0.09
Ca	0.006 to 0.08	V	3.3 to 4.3
Cr	1.8	Na	0.013

B. *Growth Mechanisms*

The fractional crystallization process aims for a low crystal growth rate, with a moving velocity of the crystallization front usually not higher than 2.5 mm min^{-1}.[6] This growth rate is necessarily low to allow enough time for the impurities segregated during the crystallization to diffuse into the liquid phase. In addition, the lower growth rates enable the formation and stabilization of cellular or even planar growth interface. Under high growth rate conditions or high concentration of solutes, a dendritic growth interface will be formed. This ultimately leads to a poor refining performance due to the excess solute entrapped between the dendrite arms.[14]

1. *Growth interface morphology*

The growth interface morphology is mostly driven by the growth conditions, such as the constitutional supercooling, growth rate, and temperature gradient at the solid–liquid interface. Supercooling during the growth induces different interface morphologies of the solid at the crystallization interface, such as planar, cellular, or even dendritic form (see Figure 1).[15]

A planar growth morphology can be achieved in a situation with low supercooling, low solute concentration, and a low growth rate. These are usually the conditions adopted during crystal growth and fractional

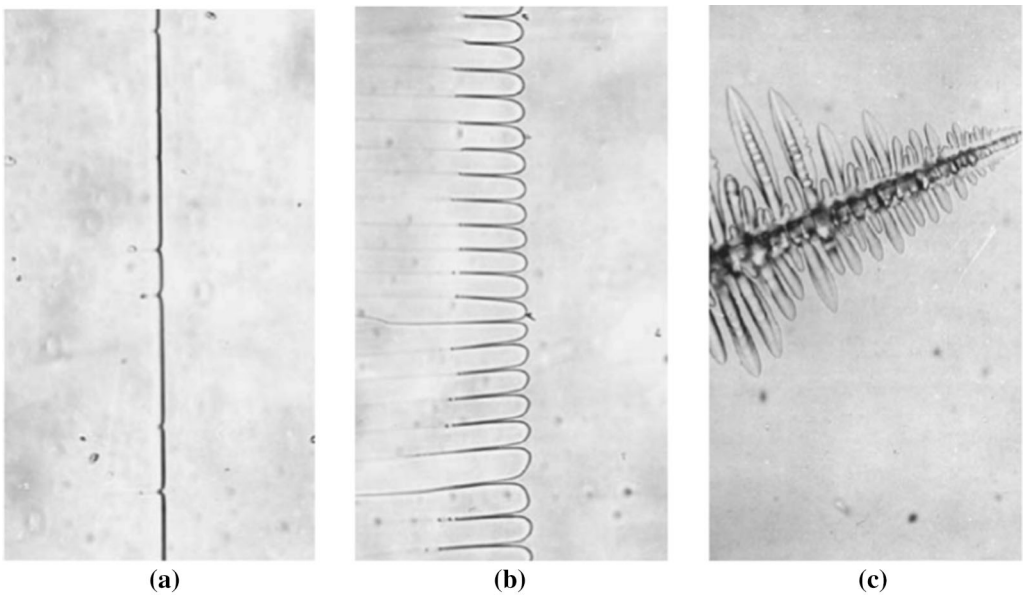

Fig. 1—Representation of a (*a*) planar, (*b*) cellular, and (*c*) dendritic interfaces. Reprinted from Ref. [15] with permission from Elsevier.

solidification processes. On the other hand, at the boundaries of the forming crystals (where the solutes with $k < 1$ are segregated), the melting point is lower in comparison with the center of the crystals. Therefore, these cells will grow more at their center, forming solute-rich channels along their boundaries. This growth morphology is characterized as cellular growth. Another growth morphology is dendritic growth. It is the worst case for refining and should be avoided at all costs. This morphology happens; *e.g.,* when the growth rate is too large, the temperature gradient is too low, or the amount of solute is too high.[14,15]

The formation of cellular and dendritic structures is not desirable for the refining as they partially entrap the solute during the crystallization, inhibiting its segregation into the melt phase. To assure a planar growth interface, and minimal supercooling, the growth rate needs to be lower than the value given by Eq. [1].[15] Aspects such as impurity type and initial concentration are also important factors on the growth interface morphology.

$$G \leq \frac{D \cdot \Delta T \cdot k}{m \cdot C_0 \cdot (1-k)}, \qquad [1]$$

G is the growth rate, ΔT is the temperature gradient in the liquid interface, m is the slope of liquidus line in the binary phase diagram, k is the distribution coefficient (C_S/C_L), D is the solute diffusion coefficient in the melt, and C_0 is the initial concentration of solute.

2. *Burton, Prim, and Slichter (BPS) model for solute segregation*

Within this model, it is considered that the impurities are partially mixed in the liquid. When the rejection of solute in the growth front is faster than the velocity, in which the solute can diffuse into the main liquid phase, an enriched layer of solute is built up ahead of the growth front. Therefore, the solute concentration in this layer—rather than the concentration of solute in the main liquid—is what determines the concentration of solute in the solid phase as the growth front advances.[16]

In this BPS model, an effective distribution coefficient (k_{eff}) is introduced. The closer k_{eff} is to k, the better purification can be achieved within the given experimental conditions.[17] Equation [2]—the BPS model—describes the effect of growth rate and the diffusion into the effective distribution coefficient (k_{eff}) for the particular case of a rotating crystal withdrawn from the melt (mostly applied for crystal pulling).[8,18]

$$\frac{C_S}{C_L} = k_{eff} = \frac{k_0}{k_0 + (1-k_0) \cdot e^{[-V\delta_{bps}/D]}}, \qquad [2]$$

$k_0 = C_S/C_0$ is the equilibrium distribution coefficient, V the solid growth rate, δ_{bps} is the thickness of the diffusion layer, and D the solute diffusion coefficient in the liquid.

According to classical fluid dynamics, the velocity of the fluid will approach zero at an interface (in this case, the solid–liquid growth front interface). That means, at the near growth interface, there will be a region of laminar flow, where its velocity is so small that the impurities can only be transported out of this region *via* diffusion. Due to this characteristic, BPS assumes that within this stagnant layer δ_{bps}, the flow velocity matches the interface growth rate (V). These assumptions are of paramount importance to predict the solute distribution in fractional crystallization, as they can be influenced by experimental conditions such as melt stirring, viscosity, and growth rate.[8,16,18,19]

3. *Boundary layer and relevant dimensionless numbers*

In the cooled finger process, a turbulent flow is introduced by the rotation of the cooled finger, see Section II–A–C. Near the solidification front, the flow can be characterized using boundary layer theory. According to Herwig,[20] this velocity boundary layer near the wall can be divided into a wall layer (often also called viscous sublayer) and a turbulent wall layer, where $\mu_t \gg \mu$ for the latter, being dynamic and turbulent dynamic viscosity, respectively. Over the thickness of the boundary layer, the flow transitions from laminar flow near the wall to laminar transport of vortices to turbulent flow. Depending on the literature, the transition region between these layers is additionally called a defect or buffer layer. An extensive theory on boundary layers can be found, for example, in Herwig[21] or Bredberg.[22]

As mentioned, the diffusion boundary layer thickness is important regarding the distribution of impurities near the solidification front. As for most liquids (especially liquid metals), the diffusion boundary layer thickness is much smaller than the boundary layer thickness, characterized by Schmidt numbers much greater than unity. The Schmidt number Sc is defined according to Eq. [3] and describes the ratio from diffuse momentum transport to diffuse mass transport.

$$\mathrm{Sc} = \frac{v}{D}, \qquad [3]$$

with v being the kinematic viscosity and D being the Diffusivity. As for higher Schmidt numbers, the momentum transport is dominant over diffusive mass transport, the mass transport perpendicular to the solidification front is highly influenced by the viscous sublayer thickness.

Similarly, the influence on the boundary layer (flow) to the temperature field can be estimated using the Prandtl number Pr, which is defined as the ratio between kinematic viscosity v (momentum diffusivity) and thermal diffusivity a.

$$\mathrm{Pr} = \frac{v}{a} = \frac{c_p \cdot \mu}{k}. \qquad [4]$$

In conclusion, for Prandtl numbers, much smaller unity thermal diffusivity dominates over momentum transport. Therefore, the temperature field is less influenced by the flow within the boundary layer.

II. SUBJECTS AND METHODS OF INVESTIGATION

For the investigation and characterization of the fractional crystallization within the cooled finger process, experimental, analytical, phase field under purely diffusive conditions at microscale and computational fluid dynamic at macroscale (CFD) simulation methods were used.

A. *Cooled Finger Process*

The experimental setup of the cooled finger purification process is illustrated in Figure 2(a). It consists of a rotating, air-cooled metallic rod inserted into a molten bath. The metallic rod is covered with a high-purity graphite shell, which prevents physical contact between the rod and the melt.

Using an A20 clay-graphite crucible coated with Boron nitride, 5.6 kg of the initial alloy material (Section II–E) was melted in an open resistance-heated furnace using Argon as protective atmosphere. At the bath mirror height of the liquid aluminum, the inner diameter of the crucible is around 150 mm. The furnace input temperature was set to 720 °C (control thermocouple located outside the muffle pipe). Once the melt reached the final processing temperature, after stirring and homogenizing the mushy melt (using this mushy state to also calibrate the type-K melt thermocouple to solidus temperature), the pre-heated cooled finger was immersed into the molten bath. After a period of temperature stabilization, the rotation was set fix and the cooling gas flow was initiated. The thermocouple near the crucible wall indicates a temperature difference with a maximum of around 1 K within the melt, Figure 2(b). After *ca.* 20 minutes in the crystallization phase, the cooled Finger was lift and the crystallized product removed.

Non-rotating investigations with several thermocouples have shown a maximal temperature difference of around 3K to 4K within the melt, near the process's end, Figure 2(c).

The main process parameters investigated were the rotation rate and the growth rate. The rotation rates investigated were 25, 35, 45, and 55 RPM. As the growth rate is indirectly influenced by the rotation rate and cooling gas flow rate, to obtain the necessary wide interval of growth rate for the BPS analysis, the cooling gas flow rate was varied from 45 to 55 L min^{-1}, for each investigated rotation rate.

For all trials conducted, a sample of the molten aluminum was taken before (designated as C_0) and after (C_L) each trial. A third sample (C_S) was later taken from the crystallized material. The samples of the cooled finger trials were analyzed by OES (spark spectrometry) at IME/RWTH, or by GDMS (glow discharge mass spectrometry) at EAG Eurofins Materials Science,

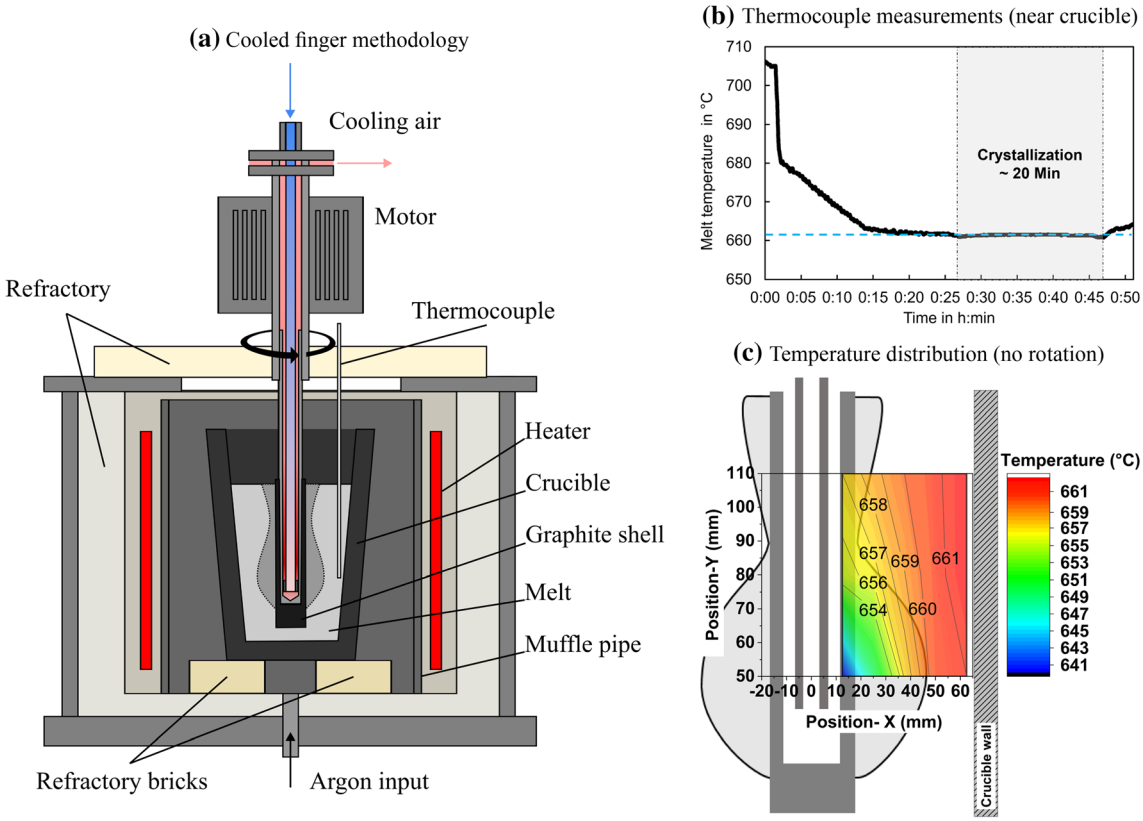

Fig. 2—Cooled finger fractional crystallization developed at IME of the RWTH Aachen University: (*a*) experimental setup for the Cooled Finger, adapted from Ref. [23]; (*b*) exemplary melt temperature measured near the crucible; (*c*) temperature distribution within the melt, interpolated from thermocouple measurements.

Toulouse—France, depending on the impurities concentration in the samples. The purification ratio achieved in the trials was calculated according to Eq. [5].

$$\text{Purificationratio} = \left(1 - \frac{C_S}{C_0}\right) \cdot 100\,. \qquad [5]$$

The average growth rate was determined by dividing the thickness of the crystallized sample by the crystallization time. To obtain the crystallization time, a thermocouple is placed inside the melt (adjacent to crucible wall) to record the melt temperature during the trials. By plotting the "temperature vs time" curve, an approximated crystallization time can be obtained from the stabilized plateau formed during the crystallization stage of the process, Figure 2(b).

1. *Thermal process design*

Within the given temperature ranges, the thermal transport between the melt/crucible and the muffle pipe is mostly driven by natural and protective gas convection. Therefore, the atmosphere within the process should be very homogenous from the beginning. Naturally, radiative and conductive losses will be higher at the top of the melt.

The heat transfer within the cooled finger is driven by forced convection, and therewith highly influenced by the geometry inside the cooled finger. To get an impression of the distribution of the heat transfer coefficient within the cooled finger, a high-resolution 3D RANS (Reynolds Averages Navier Stokes) CFD simulation was done for a symmetric quarter of the cooled finger geometry, Figure 3(a). The simulation does not include the full height of the cooled finger construction, only 3 to 4 cm over melt mirror level. The simulation used the k–ω SST (shear stress transport) turbulence model, which is a blending model between the k–omega and k–epsilon model. The graphite outer shell surface temperature was set to $T_{sol} = 933.47\,\text{K}$. The cooling gas flow was set to $50\,\text{L}\,\text{min}^{-1}$ with a temperature of 25 °C.

As it can be seen from Figure 3(c), the heat transfer coefficient between air and wall is locally very high, especially in the bottom of the cooled finger. This is not optimal and was taken care of within the next design iteration of the cooled finger (not part of this publication). Considering that the thickest part of the ingot is in the area with the highest heat transfer coefficient within the cooled finger, the simulation results show qualitatively good agreement with the solidified ingot shape, when considering the higher heat loss at the top of the melt.

The simulated temperature difference between air inlet and outlet was calculated as 365.3 K. To verify this result, the temperature difference between inlet and outlet has been measured, Figure 4(a). The measurement data, Figure 4(a), indicate that the removed heat over the phase of the crystallization is constant. Furthermore, the temperature difference measurements of the cooling air (ΔT approx 365 K at $50\,\text{L}\,\text{min}^{-1}$) within the cooled finger indicates that roughly 95 to 97 pct of the removed heat (by cooling air) are caused by the enthalpy of fusion by the liquid metal ($\Delta H_{fus} = 10.7\,\text{kJ}\,\text{mol}^{-1}$, *ca.* 18 minutes crystallization time and roughly 1 kg solidified mass), indicating that the process during the crystallization phase operates at high energy efficiency.

2. *Thermals and growth rate*

From the measurements, Figure 4(b), it can be seen that the removed heat during the process is not changing

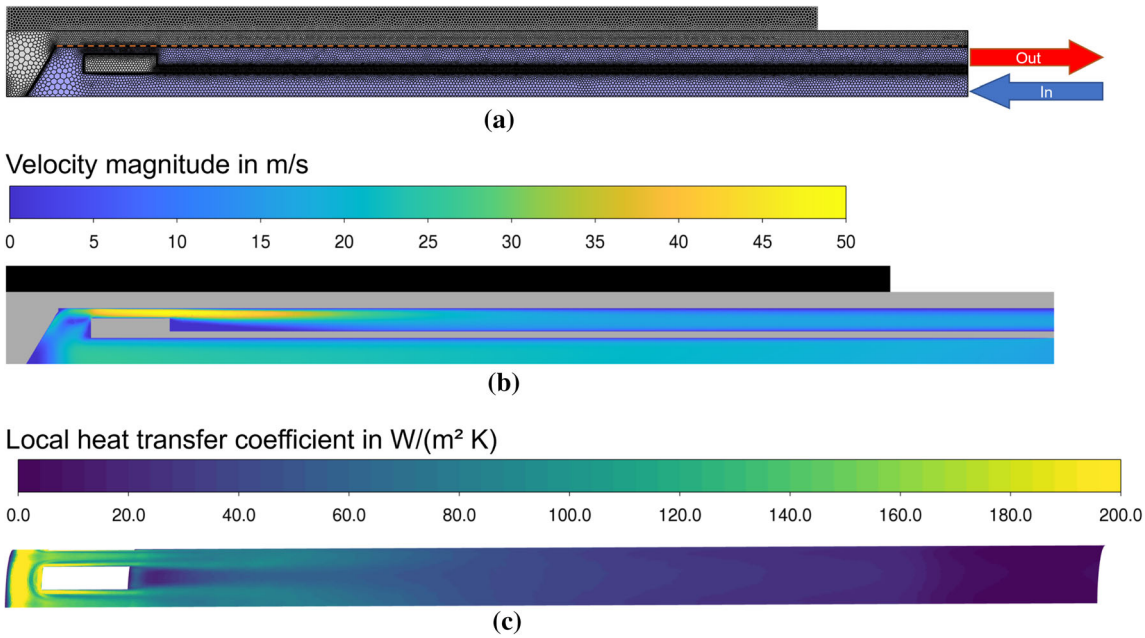

Fig. 3—CFD Simulation of the current cooled finger design airflow: (*a*) mesh—symmetry plane; (*b*) air velocity—symmetry plane; (*c*) local heat transfer coefficients (air/steel)—inside steel wall—radius dashed orange line of (a) (Color figure online).

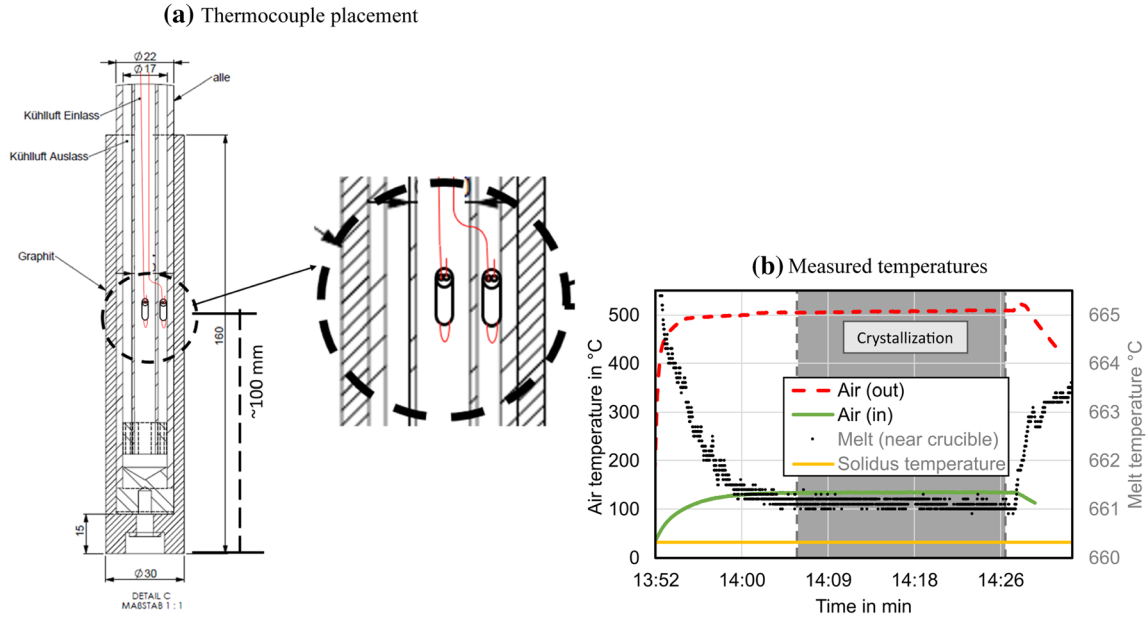

Fig. 4—Measurement of the cooling air temperatures: (*a*) thermocouple placement; (*b*) measurement data (50 L/min).

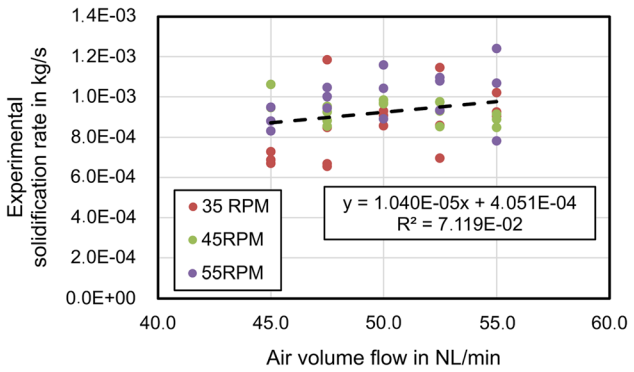

Fig. 5—Experimentally determined mean solidification rates from solidified mass and crystallization times.

significantly. This leads to the conclusion that the growing solidification front has negligible influence on the heat transfer inside the cooled finger.

During the trials, there was no online measurement of the solidification mass during the trials. Therefore, the solidification time could not be measured very accurately. As a result, the correlation shown in Figure 5 is very weak. Nevertheless, it can be seen that the influence of the rotation rate, which may increase the heat transfer between the solidified aluminum and the melt, is not significant in the range between 35 and 55 RPM. Using the regression, the solidification times for 1 kg solid for the cases 45, 50, and 55 L min^{-1} are 19.1, 18.0, and 17.1 min.

To estimate the growth rate of the solidification front during the process, a perfect radial growth starting from the inner cylinder radius at $R_i = 1.5$ cm will be assumed. A linear radial growth speed can be calculated from the final volume (solidification mass of 1 kg and $R_i = 1.5$ cm) of the hollow cylinder and the respective solidification times. For 45, 50, and 55 L min^{-1} they are 16.0, 16.9, and 17.8 μm s^{-1} respectively. As the removed heat over time is approximately constant, so it should be the increase in solidified mass over time. Therefore, these values can only be a rough estimate. Logically, due to the radial growth, it should be more accurate to use constant solidification rates and calculate the change in speed of the solidification front over the growth of the ingot. The results of this analysis, again assuming perfect cylindrical growth, are shown in Figure 6(b). Furthermore, to account for the greater deviation from this growth type within the trials, see Figure 6(a), a locally increased solidification rate will be used. The radius of the experimental shape is at maximum 7.4 pct greater than the according perfect cylindrical growth of the same mass. As the solidification rate is proportional to the outer radius squared, the necessary growth rate must locally be increased by around 15 pct. The corresponding calculated values in the Figures 6(b) and (c) are marked by the addition (inc). It can be seen that the local growth rate decreases over the solidification/process time, laying in between 32.6 and 11.6 μm s^{-1} within the trial series.

Additionally, the temperature and gradients within the solidified ingot can be estimated, using the perfect cylindrical growth approach. The heat flow in a cylindrical system can be calculated using Eq. [6].

$$\dot{Q} = 2\pi\, H\, \lambda \cdot \frac{T_{r_a} - T_{r_i}}{\ln(r_a/r_i)}, \qquad [6]$$

H is the height of the cylinder and λ the thermal conductivity of the solid. The heat flow from the experiments can be roughly estimated using the measured flow rate and the temperature difference of the cooling air, Figure 4(b). This measurement was only done for one trial at the end of the trial series (25 RPM and 50 L/min). The mean extracted heat flow during the

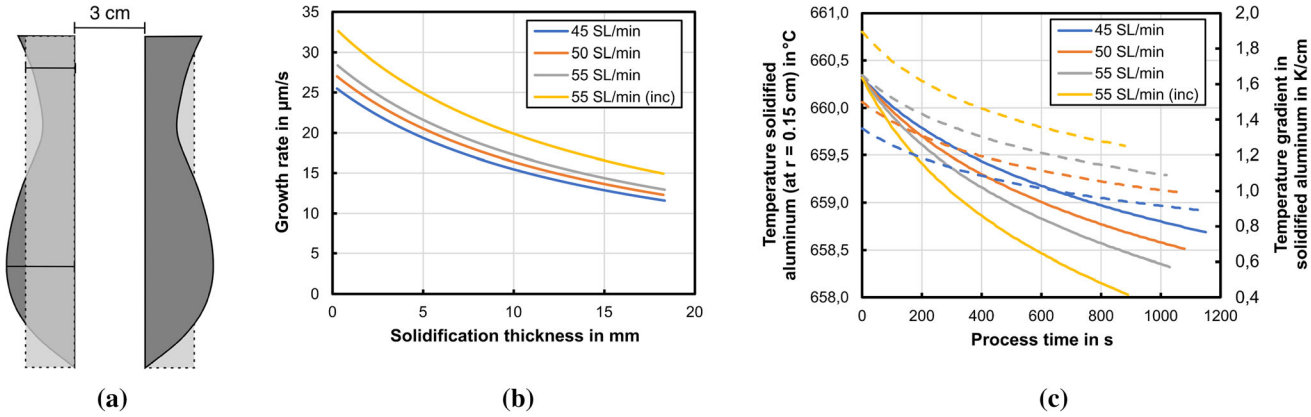

Fig. 6—Estimation of growth rates and temperature (gradients) dependent on cooling rate: (*a*) ideal shape *vs* experimental shape; (*b*) growth rates perfect cylindrical growth; (*c*) solid lines: temperatures of solidified aluminum at the graphite shell border, dashed lines: temperature gradient of the solidified aluminum.

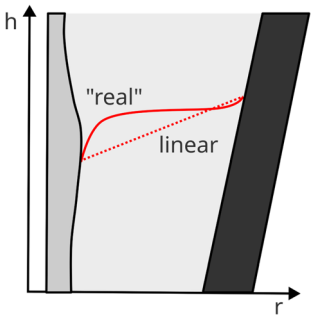

Fig. 7—Exemplary view on "real" *vs* linearized temperature gradient within the melt.

trial was 380 W. The values for the other cases were scaled according to the corresponding volume flow rates. Additionally, for the locally increased shape, (inc) was also scaled by 15 pct. The accordingly calculated temperature of the ingot at the inner radius R_i (near graphite shell of the cooled finger) is shown in Figure 6(c), so is the calculated temperature gradient using solidus temperature at the solidification front. It can be seen that also the local temperature gradient in the solid decreases of time, laying in between 0.9 and 1.9 K cm^{-1} within the trial series. It can be seen from the measurement of the melt temperature near the crucible, Figure 4(b) (melt temperature is quite constant over the crystallization phase) that the linearized gradient in the melt should be smaller than approximately 1 K cm^{-1} during the crystallization and slightly increase over the time of the process, as the solidification front (solidus temperature) moves in the direction of the thermocouple. However, it is important to note that the local gradient near the solidification front and the crucible wall will be higher than the linearized value, as boundary and flow effects must be considered within the melt. Anticipating the results from Section III–B–1, it can be seen that the Prandtl number of the liquid metal is $\ll 1$, which in this case indicates that the temperature gradient near the walls should not be near the same order of magnitude than the linearized gradient. Due to the rotation of the cooled finger and the herewith higher velocities near the solidification front than near the crucible in comparison, the temperature gradient will be steeper near the solidification front than near the crucible. This is qualitatively illustrated within Figure 7.

A reinforcing factor, which could increase the temperature gradient near the solidification front, could be the potential formation of Taylor–Couette vortices, as they would transport warmer melt near the crucible to the direct vicinity of the solidification front. Because the decrease of the growth rate is more pronounced than the decrease of the solid gradient and the liquid temperature gradient should increase over time of the process, the purification effect should qualitatively increase with the radius of the ingot (process time), which corresponds to the experimental analyses.

3. *Liquid metal flow within the process*

Due to the design of the process, the flow within the process should vary between the characteristic flow of a pure rotating Cylinder and a Taylor–Couette flow, whose are described by Childs.[24]

4. *Dimensionless analysis*

Dimensionless numbers in fluid mechanics allow it to derive conclusions about the characteristics of a flow from an experiment or a simulation of similar structure but different dimensions or material properties. Therefore, to get an impression of the nature of flow within the cooled finger process, several dimensionless numbers will be used.

The Reynolds number, Eq. [7a], characterizes the ratio between inertia and viscous forces. Its value can characterize critical points for a flow such as the change between laminar, transitional, and turbulent flow. The Grashof number, Eq. [7b], characterizes the ratio of buoyancy to viscous forces acting on a fluid near a surface. The Richardson number, Eq. [7c], characterizes if this non-isothermal flow near a surface is dominated by forced or free convection, if Ri $\gg 1$ forced convection may be ignored and Ri $\ll 1$ free convection may be ignored.

The Taylor number, Eq. [7d], is specific for the analysis of a Taylor–Couette flow type and characterizes the tendency of a flow to form Taylor vortices, where ω is the angular velocity and ν is the kinematic viscosity. This is interesting as with increasing solidified mass, the tendency to form a Taylor–Couette flow will become more pronounced, as this flow pattern, which is dominated by viscous forces, is favored by the reducing distance between the solidification front and the mold wall. As this type of flow tends to stabilize turbulent inducing effects, it can be relevant in some cases.

$$\mathrm{Re} = \frac{u_{\mathrm{char}} \cdot L_{\mathrm{char}}}{\nu}, \qquad [7a]$$

$$\mathrm{Gr} = \frac{\beta\, g \cdot (T_{\mathrm{s}} - T_{\infty})\, L_{\mathrm{char}}^3}{\nu^2}, \qquad [7b]$$

$$\mathrm{Ri} = \frac{\mathrm{Gr}}{\mathrm{Re}^2}, \qquad [7c]$$

$$\mathrm{Ta} = 4\,\frac{\omega^2}{\nu} \cdot R_{\mathrm{i}}^2 \cdot \frac{(R_{\mathrm{a}} - R_{\mathrm{i}})^3}{R_{\mathrm{a}} + R_{\mathrm{i}}}. \qquad [7d]$$

For a rotating cylinder flow, the characteristic length L_{char} is the radius of the cylinder, and the characteristic velocity u_{char} is the orbital velocity on the cylinder radius as product of angular velocity ω and radius $u_{\mathrm{char}} = \Omega \cdot R_{\mathrm{cyl}}$. For a Taylor–Couette flow with a rotating inner cylinder, the characteristic length is given as the gap size $L_{\mathrm{char}} = (R_{\mathrm{a}} - R_{\mathrm{i}})$, the characteristic velocity is the same.[24]

Having a relative complex and evolving geometry during the process, making precise analytical predictions about the flow is difficult. For a rotating cylinder, the transition from laminar flow happens roughly at a Reynolds number of around 60.[24]

Having relatively small $R_{\mathrm{a}}/R_{\mathrm{i}}$-ratios during most of the process, varying between 0.2 and 0.9 (the maximum is reached at the end of the process and only locally), a stable formation of Taylor vortices seems unlikely during most of the process. In general, the critical Reynolds number of a Taylor–Couette flow for the transition between a laminar and turbulent transitional flow can vary[25] in between different case a lot. As a rule of thumb, Reynolds numbers greater 3×10^4 to 4×10^4 can be treated as turbulent in many cases. Depending on the Taylor number, the turbulence flow structure may vary in its general structure. It is starting to become very instable and irregular for Taylor numbers in the order of 1×10^7 to 5×10^7.[26]

B. *Analytical Approach for the Determination of the Diffusion Layer Thickness from BPS*

The BPS model takes, among other parameters, the thickness of the diffusion layer, formed ahead of the growth interface, into account. This value is used to predict the achievable effective distribution coefficient (k_{eff}). This effective distribution coefficient can be experimentally obtained by dividing the concentration of impurities in the crystallized sample C_{S} by the concentration of impurities in the remaining liquid C_{L}.

The proposed Eq. [2] from BPS can be transformed in a linear equation $y = a - b \cdot x$, in a way that

$$\ln\left(\frac{1}{k_{\mathrm{eff}}} - 1\right) = \ln\left(\frac{1}{k_0} - 1\right) - V \cdot \left(\frac{\delta_{\mathrm{bps}}}{D_{\mathrm{x-Al}}}\right), \qquad [8]$$

where $k_0 = C_{\mathrm{S}}/C_0$, $k_{\mathrm{eff}} = C_{\mathrm{S}}/C_{\mathrm{L}}$, and $D_{\mathrm{x-Al}}$ is the liquid diffusion coefficient of the impurity "x" in aluminum.

Within this analytical approach, the experimental values of $ln((1/k_{\mathrm{eff}}) - 1)$ are plotted against the growth rate (V) for each level of rotation rate. It is then possible to extract the inclination and intercept coefficients by fitting the plotted values in a linear equation. Based on these coefficients, the experimental value of k_0, as well as the values of $\delta/D_{\mathrm{x-Al}}$, can be obtained. When both these obtained values for each rotation rate are inserted in the BPS equation [2] using the average growth rate of the conducted trials, it is possible to obtain the effective distribution coefficient for each rotation rate.

However, since the values of the diffusion coefficient in liquid are difficult to be obtained and differs between authors, the following analysis will treat the diffusion as a constant for each analyzed impurity, and a comparison between the combined value $\delta/D_{\mathrm{x-Al}}$ is performed among the investigated rotation rates for every selected impurity. At the end, the absolute value of diffusion layer thickness is calculated based on a literature value of the liquid diffusion coefficients for the investigated impurities in molten Al.

C. *Numerical Approaches for the Determination of the Diffusion Layer Thickness*

Due to the influence of small local quantities (in the range smaller 50 to 100 μm) close to the solidification front, *e.g.*, local temperature gradients and the diffusion layer thicknesses, which are crucial for the success of the process. The type of turbulence, which is not ideal for normally used eddy viscosity models (RANS), as these are optimally designed for a dominant vortex transport direction and no time-accurate transient initiation (URANS) of turbulent phenomenon, as well as the inherently transient properties of the process and the local quantities. The remaining reliable simulation methods to predict these local quantities are only appropriately high-resolved DNS, LES methods. These would have the additional difficulty that with the selected resolution at the edge of the solidification front, the shape of the solidification would have to be resolved additionally and a typical macroscale simplification model as for example porosity approaches (for the case of dendritic solidification) would not be valid within these orders of magnitude anymore. In addition, to represent a smooth-walled solidification, for example by an adaptive mesh would require an additional, not negligible, computational effort. Detailed simulations, which could make precise statements about the solidification state from a macroscopic view of the process

(melt flow, air flow and thermals) are, therefore not possible, or only with very high computational and research time effort.

Therefore, this paper focuses on some investigations from much more simplified problem sets to get trends of influential process parameters.

1. *2D RANS estimation of boundary layer thickness and local temperature gradients*

At first, a simple stationary 2D RANS CFD simulation of a rotating disk has been set up, with varying inner radius of 1.5, 2.5, and 3.5 cm, within a cylindrical environment, outer radius 6.5 cm. In this model, the *k*–omega SST model with curvature correction, see Reference 27, was used. The intent was to get a tendency for the laminar sublayer thickness from the pure shear flow near the solidification front, without the influences of macroscopic turbulent effects. As only the cooled finger rotates, and natural convection effects may be neglected (see section Richardson number), this should be relatively accurate estimation. A very fine mesh (*ca.* 320 k cells) was used to guarantee y-plus values $y^+ \ll 1$ near the walls, to fully resolve the velocity profile of the boundary (and sub-) layer within the mesh. For the temperature boundary conditions, the inner circumference was set to solidification temperature 933.47 K and the outer circumference was set to 934.47 K, in accordance with the experimental measurements.

The laminar sublayer was estimated by incrementally calculating the y-plus values of cells on a line directed radially outwards from the inner disk's wall, using Eq. [9a]. With u being the velocity parallel to a wall, y being the distance from the wall and τ_{Wall} being the corresponding wall shear stress.

$$y^+ = \frac{y}{\nu} \cdot \sqrt{\frac{\tau_{\text{Wall}}}{\rho}}, \qquad [9a]$$

$$\tau_{\text{Wall}} = \mu \left. \frac{\partial u}{\partial y} \right|_{y=0}. \qquad [9b]$$

As the y^+ value starts from $\ll 1$ and the wall distance y is only slightly increased by each cell, this should be a relatively accurate estimation within the sublayer. According to most literature, the boundary between sublayer and buffer-layer is defined at $y^+ = 5$. Therefore, the radial cell wall distance of the first cell $y^+ \geq 5$ will be used as estimated sublayer thickness.

2. *3D RANS estimation of boundary layer thickness and local temperature gradients*

To estimate differences between an isothermal 2D and a thermal 3D RANS simulation, an additional 3D simulation was made using the final-solidified ingot shape, Figure 6(a). Therefore, also the *k*–omega SST model also with curvature correction was used. The mesh with around 865k cells is shown in Figure 8(a). As for the 2D simulations this mesh is well resolved near the walls with $y^+ \leq 1$.

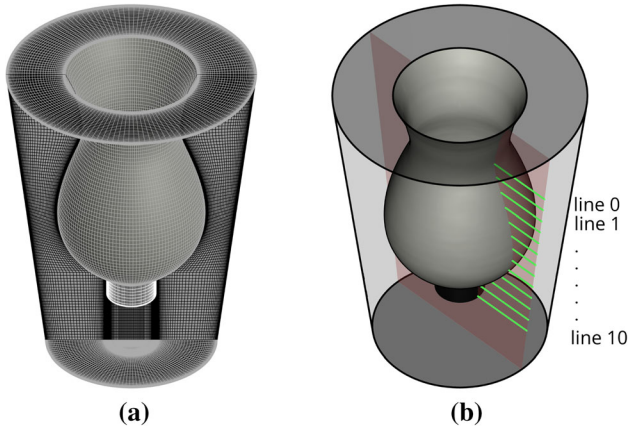

Fig. 8—Mesh of thermal 3D RANS simulation (*a*) and the lines (numbered 0 to 10 from top to bottom) for evaluation of laminar sublayer thickness (*b*).

The circumferential crucible temperature was set to 934.47 K, and the solidified ingot surface was again set to solidus temperature. A rotation speed of 55 RPM was used within the simulation. The top of the surface was set to a mixed thermal boundary condition with a heat transfer coefficient of 10 W/(m^2 K), an emissivity of 0.2, and an environment temperature of 933.15K. All other surfaces were set as perfect thermal insulator.

3. *LES simulation of solute impurity distribution*

At least a multi-zone LES/DES (Large/Detached Eddy) simulation to deliver a qualitative estimation of turbulent diffusion layer effects from the rotation rates of 25RPM. Therefore, a rotating cylinder $R_{\text{I}} = 0.015\,\text{m}$ within an outer cylinder $R_{\text{A}} = 0.065\,\text{m}$ was modeled over a height of 5cm. The resulting mesh has around 48 million cells, Figure 9.

The top and bottom walls were modeled as shear-free walls. The DES model available within ANSYS Fluent was used to avoid high resolution of near wall region at the outer cylindrical wall, as this was not the main region of interest. Within the LES zone, the WMLES S-omega model was used, which is a blending of a modified Smagorinsky sub-grid turbulence model, a mixing length model and a y-plus value-based wall-damping model, see Reference 27. In contrast to standard LES, the WMLES approach has the benefit of allowing cell aspect ratios greater unity very close to the wall (within roughly maximal 10pct of the boundary layer).[28] Within the DES zone, an enhanced shielded Delayed Detached Eddy Simulation (DDES) approach was used.

To start the simulation, 7800 time steps ($\Delta t = 0.002\,\text{s}$) were simulated, which corresponds to 6.5 rotations at the set rotation speed of 25 RPM.

In the following, the diffusion was modeled using the general scalar transport equation (10) for the scalar property ϕ_k.

$$\frac{\partial(\rho\,\phi_k)}{\partial t} + \frac{\partial}{\partial x_i}\left(\rho u_i \phi_k - \Gamma_k \frac{\partial \phi_k}{\partial x_i}\right) = S_{\phi_k}\; k = 1, \dot{s}, N. \qquad [10]$$

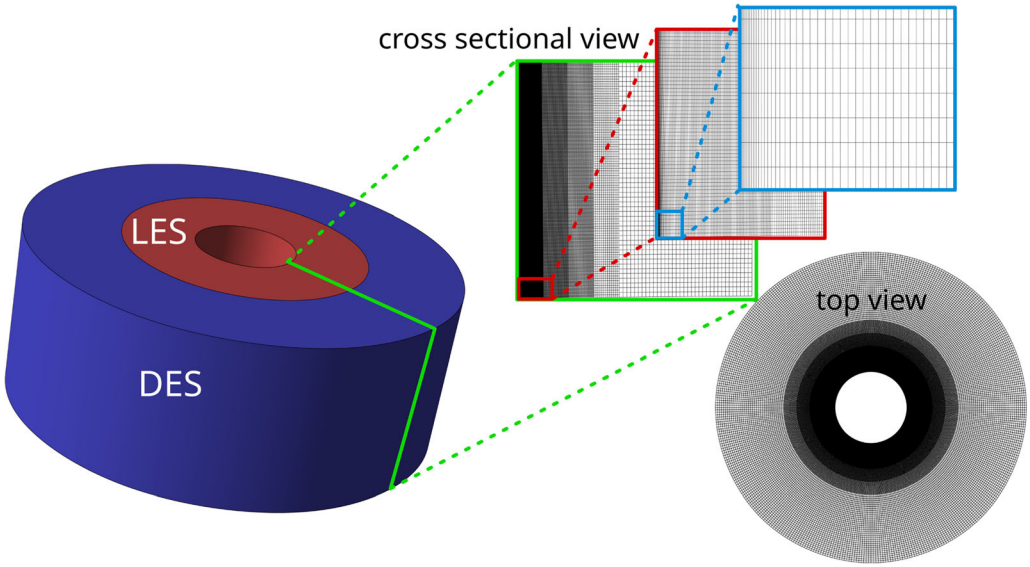

Fig. 9—Mesh of the multi-zone LES/DES simulation.

Table II. Derived Scalar Transport Values to Model the General Diffusive Behavior of the Different Impurities Within the LES Simulation

	Unit	Pb	Fe	Si
c_{0,ϕ_k}*	wt	5.00×10^{-4}	3.00×10^{-6}	2.00×10^{-5}
j_{ϕ_k}	kg s^{-1} m^{-2} 1.00×10^{-4}	5.00×10^{-7}	4.00×10^{-6}	
Γ_k	kg s^{-1} m 1.03×10^{-5}	3.62×10^{-6}	7.54×10^{-6}	

Comparing Eq. [10] to the general diffusion equations the scalar diffusivity Γ_k can be calculated according to Eq. [11] from the temperature-dependent diffusion coefficient D_T.

$$\Gamma_k = \rho \cdot D_{T,k}. \quad [11]$$

As boundary condition for Eq. [11] the flux of the scalar ϕ_k through a surface A can be given by Eq. [12] within the CFD software.

$$j_{\phi_k} = \frac{d\phi_k}{dt} \cdot \frac{1}{A} \quad [12]$$

Some simplifications are being used to model the local enrichment of impurity elements like Fe, Pb, Si.

1. Constant mass source of impurity elements, calculated from experimental data, in the cells near the cooled finger side walls (inner cylinder).
2. Initializing with original concentration of elements C_0

As diffusive transport is not only influenced by the diffusivity, but also by the concentration gradients, an approximate modeling of the real concentration conditions in the process is necessary. Therefore, experimental results of several trials were evaluated and averaged for the usage in the LES simulations, see Table II.

The shown boundary fluxes were applied after 7800 timesteps. Additionally, at 15000 timesteps, the rotation rate was changed to 55 RPM, to see the qualitative effect of higher rotation rate to the transient distribution of the scalars.

D. *Phase Field Simulations*

The results of simulations presented here derivate from previous work published in Reference 29. Through a combination of microstructure simulations on a mesoscopic scale and macroscopic temperature field simulations, this paper[29] demonstrates how phase field simulations can be used to investigate the influence of process parameters on the cooled finger process refinement for aluminum. The simulations in Reference 29 were performed considering aluminum with the common impurity elements manganese, iron, and silicon. In this work, we have replaced manganese with lead to mimic the experimental measurements.

The 2D simulations presented are performed using the software MICRESS[30] which is based on the multiphase field model and linked to thermodynamic databases.[31,32] The thermodynamic calculations are based on Thermo-Calc using the database TCAL6.[33] Phase field software combines microstructure simulation with a macroscopic temperature solver on the process scale using a 1D-macro model, providing a direct coupling

between the global heat flow and the local latent heat release.[29,34]

The microstructure simulation domain is rectangular and has a size of 1 x 1.5 mm^2 with a grid resolution of $\Delta x = 1$ μm. The 1-dimensional macroscopic temperature field has a total length of 10 cm which corresponds to the geometry of the experimental device. The total simulated time is 1200 seconds. A fixed concentration equal to the impurity element initial concentration is set on the top boundary for each element. We have studied a range of growth rates from 6 to 24 $\mu m\ s^{-1}$ and temperature gradient from 2 to 16 K cm^{-1}. The initial concentration of each of the impurities is given in Table III.

The domain was allowed to follow the solidification front with a variable distance of 511, 383, 212, and 176 μm between the solid/liquid interface and the upper domain boundary, these values corresponding the diffusion layer thickness for rotation rates of 25, 35, 45, and 55 RPM, respectively.

Table III. Nominal Alloy Composition C_0 and Segregation Coefficients k of the Impurity Elements for Phase Field Simulations

Element	Pb	Fe	Si
C_0 [wt pct]	8e−2	1.4e−3	5.2e−3
k	0.12	0.022	0.10

The k values vary slightly during simulation due to changes in local conditions during transformation.

Table IV. Chemical Analysis (GDMS) of the 4N8 Purity Aluminum Used to Produce the Synthetic Alloy

Elements	Concentration (ppm)	Elements	Concentration (ppm)
Si	3.37	Cr	< 0.10
Fe	1.02	Zn	< 1.00
Cu	0.61	Sn	< 0.30
Mn	< 0.10	Zr	< 0.05
Mg	0.77	Bi	< 0.70
Ti	< 0.10	In	< 0.30
Pb	< 0.20	V	< 0.20
La	0.140	Ce	0.217
Ag	< 0.01	Li	< 0.02
P	1.58	Ni	< 0.20
Ca	< 0.20	Be	< 0.01
Na	0.10	Sb	< 0.80
Ba	< 0.04	Sr	< 0.03
B	< 0.20	Cd	< 0.10
Ga	< 0.10		

Table V. Thermophysical Properties of Liquid Aluminum Near Liquidus Temperature from Refs. [35, 36]

Density ρ [kg K^{-1}]	Spec. Heat Capacity c_p [J kg^{-1} K]	Heat Conductivity λ [W m^{-1} K]	Kinematic Viscosity v [$m^2\ s^{-1}$]
2391	1127	89.27	5.62×10^{-7}

E. *Initial Material and Its Properties*

Within this study, Pb was artificially added as the main investigated impurity in a concentration of *ca.* 0.1 wt pct. The impurities Si and Fe, which are intrinsically present in the 4N8 aluminum at the ppm range, were also investigated, and their initial concentration in the 4N8 aluminum can be seen in Table IV.

For the flow simulations, the material properties listed in Table V were used. Diffusive properties, Table VI, are assumed with values taken from Viardin *et al.*[29]

III. RESULTS

A. *Diffusion Layer Thickness Model from BPS*

The experimental determination of the δ/D_{x-Al} coefficients, based on the analytical approach from the BPS model, was conducted for the impurities Pb, Fe, and Si. In the following section, the detailed results for Pb will be shown. This impurity was chosen due to its lowest distribution coefficient (close to 0), which eliminates as much as possible the influence of the distribution coefficient on the results. The main results obtained for the impurities Fe and Si, obtained *via* the same analysis, are shown in appendix, and will be summarized afterwards as well.

1. *Lead*

The obtained results of the BPS analysis for Pb can be seen in Figure 10, where the linear fitting of the plotted experimental data showed a decrease in the obtained δ/D_{Pb-Al} coefficient, when the rotation rate is increased. This can be clearly seen by the gradual decrease in the inclination of the fitted line, where this inclination (representing the $(-)\delta/D_{Pb-Al}$ coefficient) has a value of 0.133 42 for the trials conducted at 25 RPM, 0.100 06 at 35 RPM, 0.055 37 at 45 RPM, and 0.046 20 at 55 RPM.

Table VI. Diffusion Coefficients[29] and Therewith Calculated Schmidt Numbers for Liquid Aluminum Near Liquidus Temperature

	Unit	Fe	Mn	Si	Pb
D_0	$m^2\ s^{-1}$	2.34×10^{-7}	1.93×10^{-7}	1.34×10^{-7}	3.83×10^{-9}
E	J mol^{-1}	4.0×10^4	3.1×10^4	3.0×10^4	0
D	$m^2\ s^{-1}$	1.34×10^{-9}	3.54×10^{-9}	2.79×10^{-9}	3.83×10^{-9}
Sc	—	416	158	200	147

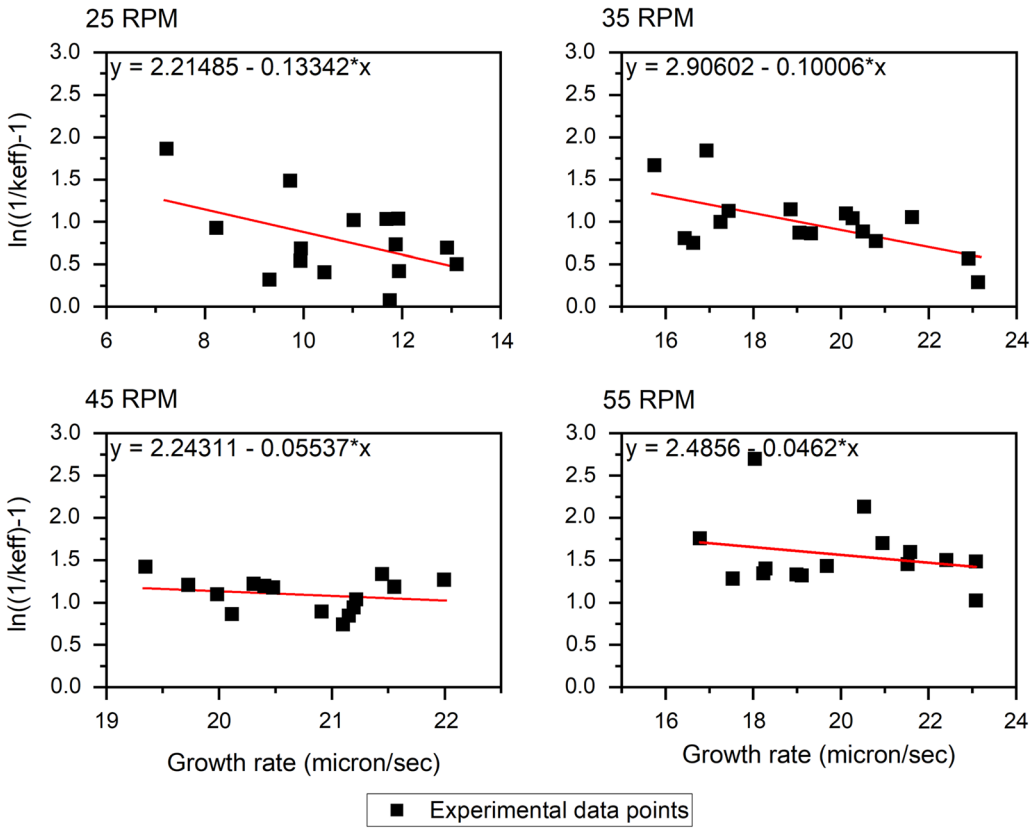

Fig. 10—BPS analysis showing the linear fitting of the obtained growth and k_{eff} experimental data for the removal of Pb. Each graph represents the trials conducted at different rotation rates.

Considering that the diffusion coefficient remains constant, a 65 pct decrease in the thickness of the diffusion layer can be achieved when the rotation increases from 25 to 55 RPM.

The decrease in this coefficient (δ/D), when a higher mixing degree is used in the trials, is foreseen in this model and fits with the obtained results from other fractional crystallization methodologies. The reason is that at higher rotation rates, higher forced convection is employed in the system. This convection promotes the removal of the impurities at the growth interface, causing the thickness of the impurity build-up layer (diffusion layer) to be decreased. The end effect is that the impurities can diffuse throughout this region in a shorter time, increasing the purification effectiveness.

When analyzing the linear intercept of the plotted data for all the investigated rotation rates from Figure 10, it is possible to observe that the lines cross the y-axis at similar values, ranging from 2.2 for 25 RPM to 2.9 for 35 RPM. This translates into an experimental value of k_0 of 0.098 for 25 RPM and 0.052 for 35 RPM, representing a maximum theoretical purification ratio varying from 90.2 to 94.8 pct.

2. *Relation between the δ/D_{Pb-Al} with the purification rate*

A better illustration of the effect of this coefficient can be seen in Figure 11, where the obtained coefficients for the BPS and are plotted against the range of purification for each applied rotation rate. For that, it is again possible to observe the effect of decreasing the diffusion layer thickness by means of rotation. The resulting effect is a pronounced increase in the achieved reduction factor of Pb in aluminum.

The increase in mixing promoted by the rotation of the cooled finger induces the removal of the expelled solute from the growth interface towards the bulk melt. By expelling the segregated solute away from the growth front, the resulting effect is a pronounced increase in the achieved reduction factor of Pb in aluminum. This can be seen in Figure 11, where, by practically reducing in two-thirds the BPS coefficient from 25 RPM to 55 RPM, the removal of Pb increased from a median value of 62 up to 77 pct, respectively.

3. *Influence of rotation rate on the values of k_{eff}*

Figure 12 shows the effect of the rotation on the obtained values of effective distribution coefficient k_{eff}, following the BPS model. These values were calculated based on the corresponding $\delta/D_{\text{Pb-Al}}$ coefficient, as well as the average of k_0 and growth rate from the experiments for each rotation rate.

In addition, the experimental range of k_{eff}, obtained for each interval of rotation rate, is plotted as a gray area in the graph. It is noted that the calculated values of k_{eff} meet the experimental range. Moreover, the literature value of k is plotted as a dotted line. This serves as an indication of how near the experimental

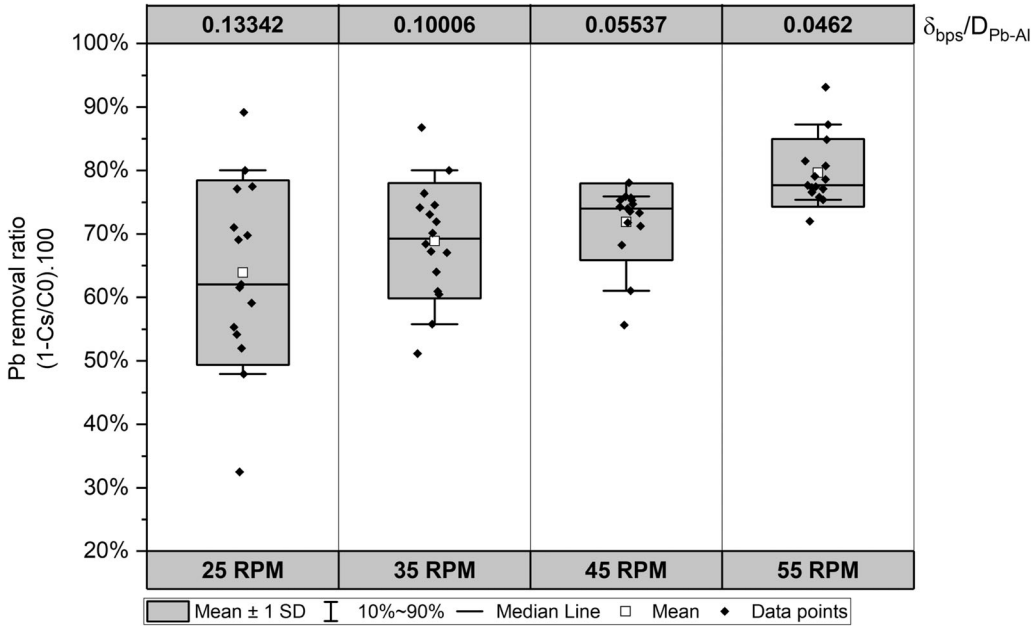

Fig. 11—Influence of the diffusion layer thickness on the obtained Pb removal ratio from aluminum.

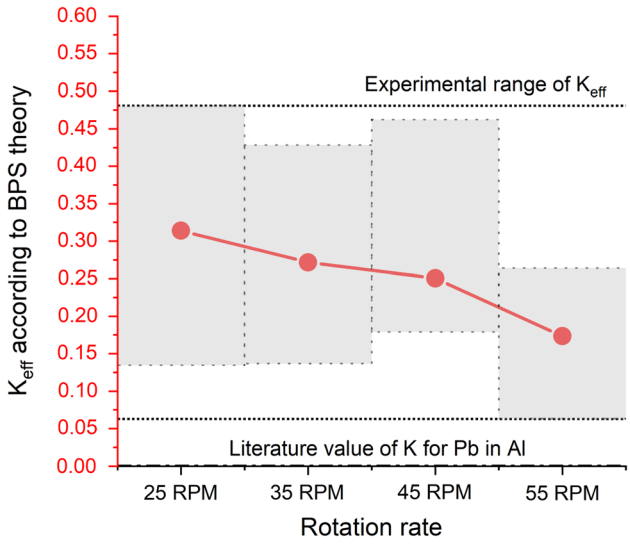

Fig. 12—Effective distribution coefficient of Pb (according to BPS theory) as a function of rotation rate (Color figure online).

values are from the theoretical values of k. The calculated k_{eff} from the BPS model shows a decreasing tendency as the rotation increases (as seen in Figure 12—red line).

4. *Summary of results for Pb, Fe, and Si*

Considering the diffusion coefficient of Pb, Fe, and Si in liquid aluminum as 3.83×10^3, 1.35×10^3 and 2.80×10^3 μm s^{-1} respectively,[37] the absolute values obtained for the diffusion layer thickness, for each experimental rotation rate, are shown in Table VII below. In this table, the k_{eff} and the $\delta/D_{x-\text{Al}}$ results for the impurities Fe and Si were added as well.

B. *Fluid Dynamic Flow Investigations*

1. *Analytic estimation of the flow regimes*

To get a rough impression of the flow regimes within the process, several dimensionless numbers introduced in Section II–A–3 were evaluated. For the rotating cylinder and Taylor–Couette flow, R_{cyl} was varied between 1.5 and 6.0 cm. For the case of the Taylor–Couette flow additionally R_{a} was modified between 6.0 and 7.5 cm. Additionally, the temperature difference between surface and mean flow temperature for the calculation of Gr/Ri was assumed with 1 K. The ranges of the dimensionless numbers are listed in Table VIII.

From the resulting ranges, it can be seen that free convection effects may be neglected and turbulent, at least turbulent transitional, flow should predominate within the melt.

The Prandtl number near liquidus temperature is around 0.017, which means that the temperature field near the solidification front should be dominated *via* heat conduction.

From the Schmidt numbers listed in Table VI, it can be seen that in contrary, the distribution of solute impurities will be dominated by momentum transport (melt flow).

2. *2D RANS boundary layer estimations*

The results from the 2D y-plus-based sublayer thickness analysis are shown within Table IX. The thickness of the laminar boundary layer represents only a kind of estimate for the real diffusion thickness, because for higher Schmidt numbers already a laminar vortex transport, as it can occur in the outer region of the laminar sublayer, represents a significant increase of the practically achieved diffusivity in such a region. It is, therefore, difficult to define a sharp limit for such a value.

Table VII. Summary of the Values Obtained from the BPS Analysis for the Impurities Pb, Fe, and Si at Different Rotation Rates

Impurity	Rotation (RPM)	δ/D_{x-Al}	k_{theory}	k_{eff}	δ_{bps} μm)
Pb	25	0.13342	0.0007 to 0.093	0.3138	511
	35	0.10006		0.2717	383
	45	0.05537		0.2506	212
	55	0.04620		0.1733	177
Fe	25	0.2503	0.018 to 0.053	0.4366	338
	35	0.4617		0.2629	623
	45	0.188		0.2330	254
	55	0.0557		0.2345	75
Si	25	0.14720	0.082 to 0.12	0.3657	413
	35	0.20150		0.2951	565
	45	0.12360		0.2773	346
	55	0.01680		0.2458	47

Table VIII. Possible Range for Reynolds, Richardson, and Taylor Numbers for Different Flow Configurations, assuming Pure Rotational Cylinder or Taylor–Couette Flow Types, Within the Process

	RPM			
	25	35	45	55
Cylinder				
Re_{max}	2×10^4	2×10^4	3×10^4	4×10^4
Re_{min}	1×10^3	1×10^3	2×10^3	2×10^3
Ri_{max}	1×10^{-2}	6×10^{-3}	4×10^{-3}	2×10^{-3}
Ri_{min}	3×10^{-3}	2×10^{-3}	9×10^{-4}	6×10^{-4}
Taylor–Couette				
Re_{max}	7×10^3	9×10^3	1×10^4	1×10^4
Re_{min}	1×10^3	2×10^3	2×10^3	3×10^3
Ri_{max}	5×10^{-2}	2×10^{-2}	1×10^{-2}	1×10^{-2}
Ri_{min}	3×10^{-4}	2×10^{-4}	9×10^{-5}	6×10^{-5}
Ta_{max}	7×10^7	1×10^8	2×10^8	3×10^8
Ta_{min}	3×10^5	6×10^5	9×10^5	1×10^6

It can be seen that the results tend to agree with the experimental values, in the context that a significant reduction takes place, but the magnitudes themselves do not agree very precisely. However, because most of the samples were taken at the outer edge near the point of the greatest growth, it is also to be expected that the experimental results are, on average, too optimistic with respect to the average value of the diffusion layer thickness.

In Figure 13, the temperatures (a) and gradients (b) over a radial probe line are shown. It can be seen that the temperature curves are very linear as expected. However, the gradients increase slightly near the "solidification front."

3. *3D RANS simulation*

The results for the laminar sublayer thickness estimation over the probe lines (Figure 8(b)) are shown within Table X.

These values are much closer to the measured values, which means that 3D flow and turbulent effects have some relevance for the estimation of the diffusion boundary layer. The temperature distribution in the vertical cross section of the simulation is shown in Figure 14(a). The velocity magnitude and the vertical flow formation can be seen in Figure 14(b). The formation of upper and lower vertical vortices can be observed. However, velocities within the vertical plane (magnitude of axial and radial velocities) are two orders of magnitude smaller than the tangential velocities near the solidification front.

From Figure 15(a), at the end of the process, the radial temperature profiles vary significantly. Furthermore, the distribution of gradients at the end of the process can be clearly seen (Figure 15(b)), due to the sensitivity of the process to the temperature gradient is not optimal. In addition, the most influencing parameter of the temperature gradient is the distance to the wall (which due to the boundary conditions is the prescribed linear gradient between $T_{Crucible}$ and $T_{solidus}$).

4. *LES simulation*

To get an impression of the type of vortices in a flow, the Q-criterion can be used. Q is calculated at half of the difference between the squared vorticity magnitude and the squared strain rate tensor within the flow field. Positive values of Q indicating areas where the vorticity dominates and negative values indicating strain rate or viscous stress-dominated areas in the flow field.The isosurfaces for $Q = 0.1$ (Figures 16(a) and (b)) and $Q = 10$ (Figures 16(c) and (d)) are shown in Figure 16. From the figures, it can be seen that the vortex formation follows the induced rotation of the flow. No stable secondary, for example, Taylor vortex structures, seem to be relevant within this configuration.

The results support the hypothesis that the induced rotation, at least at the beginning of the process, does not cause any effects that could lead to a significant local reduction, for example, of the temperature gradient between the mold wall and the solidification front.

The qualitative influence of the flow on the diffusive distribution of the elements can be estimated from the results shown in Figure 17. Here, the results of the scalar diffusion of the element lead in the LES simulation are compared with a 1D finite difference simulation, *i.e.,* Fick's second law of diffusion, for radial direction in

cylindrical coordinates. For this comparison, the 24 radial line trajectories distributed over the axially centered region (plot of the evaluation lines in Appendix) of the LES simulation were extracted and averaged.

The results shown in Figure 17 show that about 10 seconds after the switching of the rotation rate, a more significant reduction of the diffusion layer is seen than during the first 14 seconds after the start of the UDS addition at 25 RPM. This shows that the switch between 25 and 55 RPM has major influence on the diffusion layer thickness. This effect caused by the change of the flow is also visible by the qualitative comparison of the Q isosurface values between Figures 16(c) and (d).

C. *Phase Field Simulations Results*

On the Figure 18, we have plotted the results of the BPS analysis for lead for phase field calculations and experimental results (Figure 10). We have measured k_{eff} by dividing the concentration in solid (averaged between 25 and 75 pct of the total solidified length) and the nominal concentration. Below 25 pct, the initial transient of the solidification process is observed, and above 75 pct, there is residual liquid. One can see that for 25 RPM, the best approximation for the experimental results is point A corresponding to a temperature gradient of 16 K cm^{-1} and a growth rate of 10 μm s^{-1}. For the cases at 35, 45, and 55 RPM, the best approximations for experimental results are given by points B, C, and D, respectively, all corresponding to a temperature gradient of 16 K cm^{-1} and a growth rate of 18 μm s^{-1}.

In Figure 19, we have plotted the spatio-temporal evolution of the Pb-concentration field for the four different parameters sets (A, B, C, and D each have a temperature gradient of 16 K cm^{-1}). Each map shows the frozen concentration field which is moved out line by line according to the moving computation domain (marked by the green rectangle). The results were presented after a growth time of 1200 seconds for the case A and 670 seconds for the case B, C, D in order to have the same solidified length. One can see that for the different cases, the length is longer than 1 cm and almost the same. We see also for each case concentration inhomogeneities at early stage corresponding to the initial destabilized interfacial growth, but at the end, the interface is planar. Only for the case B, we can remark inhomogeneities of concentration in the solid, which corresponds to a destabilization of planar growth during solidification. For the case A, C and D despite the initial

Table IX. Results from the 2D RANS Simulation y-plus Based Sublayer Thickness δ_{SL} Analysis

	R_i		
	1.5 cm	2.5 cm	3.5 cm
25 RPM	1181μm	985μm	762μm
55 RPM	612μm	454μm	379μm

Table X. Results from Discrete Lines of the Thermal 3D RANS Simulation

line no	z_{axial}[a] A in cm	R_i in cm	δ_{SL} in μm	v_{tan} in m/s
0	– 3.7	2.91	238	0.168
1	– 4.7	3.06	228	0.176
2	– 5.7	3.44	133	0.198
3	– 6.7	3.81	114	0.220
4	– 7.7	4.12	156	0.237
5	– 8.7	4.33	135	0.250
6	– 9.7	4.43	120	0.255
7	– 10.7	4.38	108	0.252
8	– 11.7	4.07	155	0.235
9	– 12.7	3.40	172	0.196
10	– 13.7	2.31	274	0.133

R_i: Radius of solidified wall (shape) at line height, v_{tan}: tangential velocity at R_i, z_{axial}: axial coordinate below melt mirror, δ_{SL}: laminar sublayer thickness[a]Below melt level

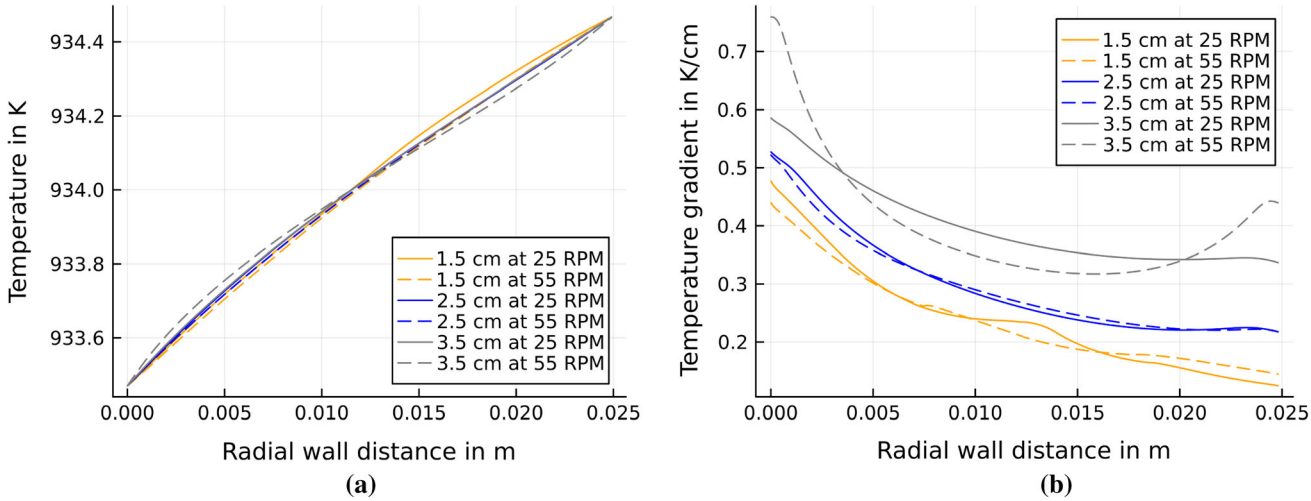

Fig. 13—Temperature curves for the 2D RANS simulations (*a*) and correspondingly calculated temperature gradients (*b*).

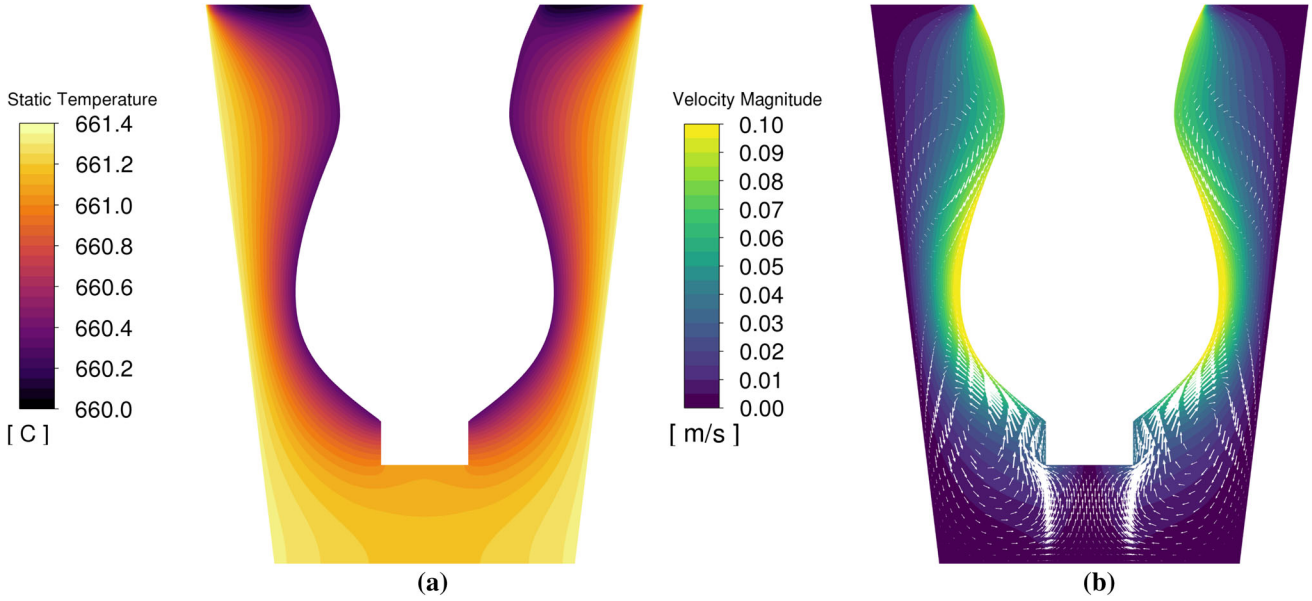

Fig. 14—Temperature distribution (*a*) velocity magnitude distribution, and in plane velocity orientation (*b*) in the vertical symmetry plane of the 3D RANS simulation.

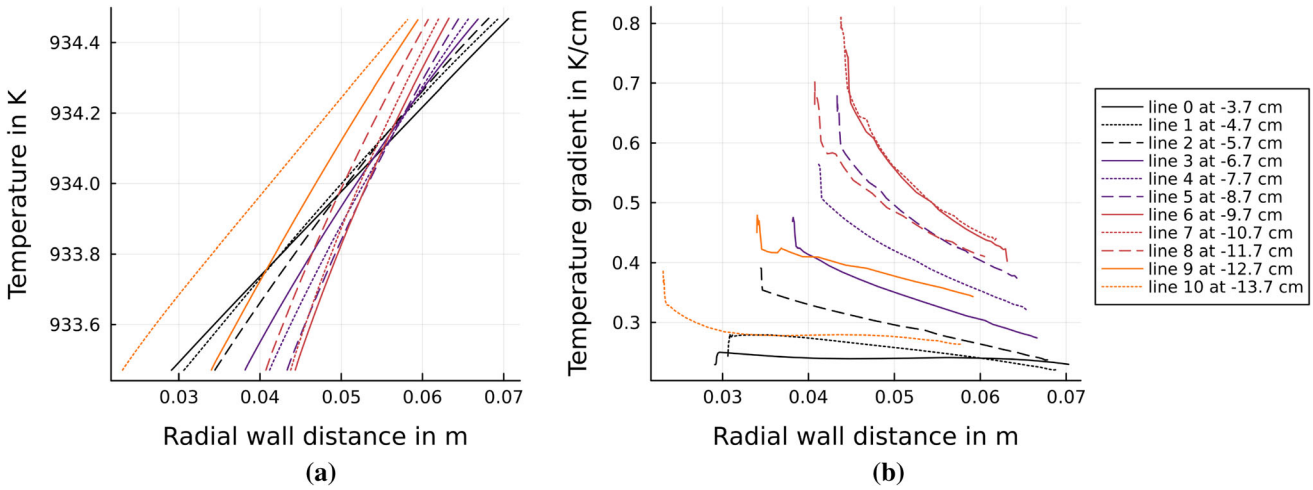

Fig. 15—Temperature curves for the 3D RANS simulations (*a*) and correspondingly calculated temperature gradients (*b*).

destabilization, the interfacial growth has remained planar. In Figure 20, we have plotted the spatio-temporal evolution of the Pb-concentration field for the four different parameters sets (the same as for figure 19 but with a temperature gradient of 2 K cm^{-1}). One can see that in these cases, the microstructures are almost cellular. Only the case A with the lower velocity ended with a planar morphology but with an almost cellular microstructure. Lower pulling velocities and higher temperature gradient are needed to maintain a planar microstructure and even for small difference in temperature gradient and pulling velocities, strong microstructural changes can be observed.

On Figure 21, we have plotted the Pb-concentration profile as function of z. For the four cases (with G = 16 K cm^{-1} from the Figure 19), at the beginning, the profile is not flat due to the initial oscillations but after longer times, all profile in solid remains flat except for the case (B) which shows oscillations. We can see that for the smaller value of rotation rates, for example, 25 and 35 RPM, the refinement is not good as for 45 and 55 RPM which confirm the experimental observation. The refinement is better at 55 RPM than at 45 RPM, nevertheless the difference between solid concentration at 55 and 45 RPM is not so important as between 45 and 35 RPM. One can also remark that refinement is better for the case D which is obtained for a time of 670 seconds than for the case A which is obtained at 1200 seconds. The gradient is the same for the both, which means that in terms of energy consumption, the case D is less energy consuming. In Figures 22 and 23, we have plotted the Si and Fe-concentration profiles as function of z, respectively. The observations are the same as for Pb, at the difference for

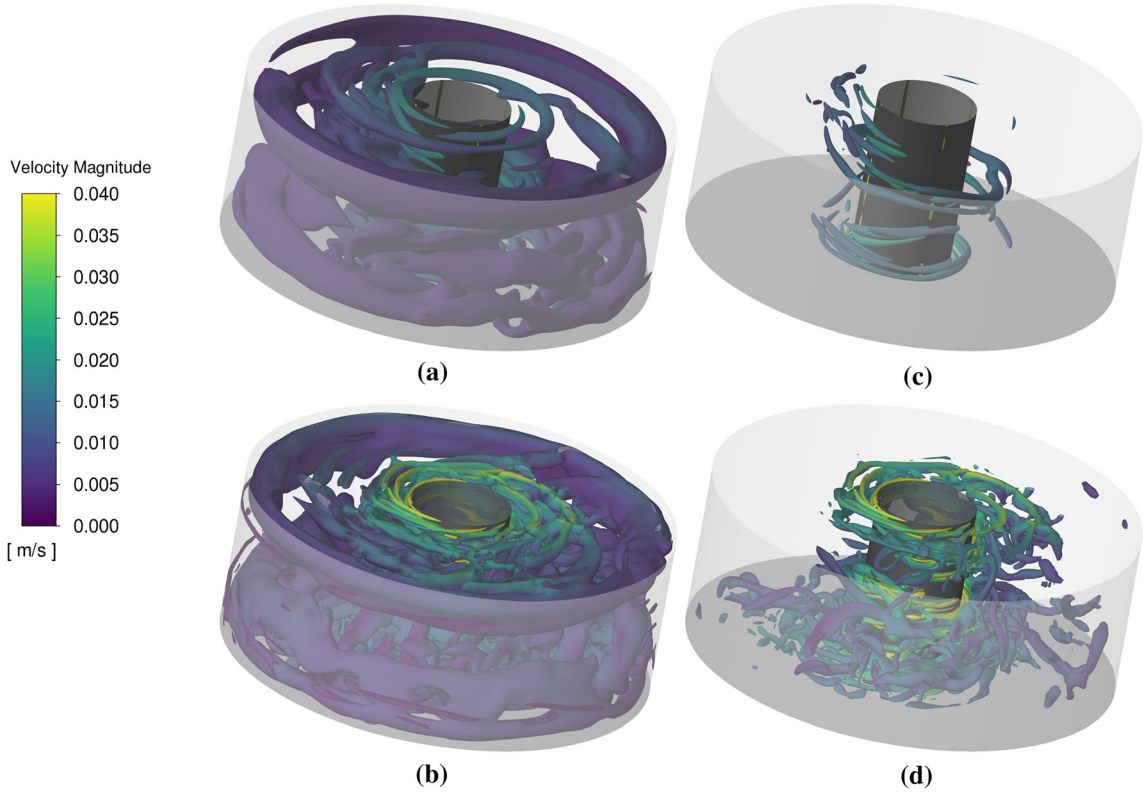

Fig. 16—Isosurfaces from Q-criterion of the LES simulation: (*a*) $Q = 0.1$ at a flow time of 30 s and 25 RPM, (*b*) $Q = 0.1$ at a flow time of 40.8 s and 55 RPM, (*c*) $Q = 10$ at a flow time of 30 s and 25 RPM, (*d*) $Q = 10$ at a flow time of 40.8 s and 55 RPM.

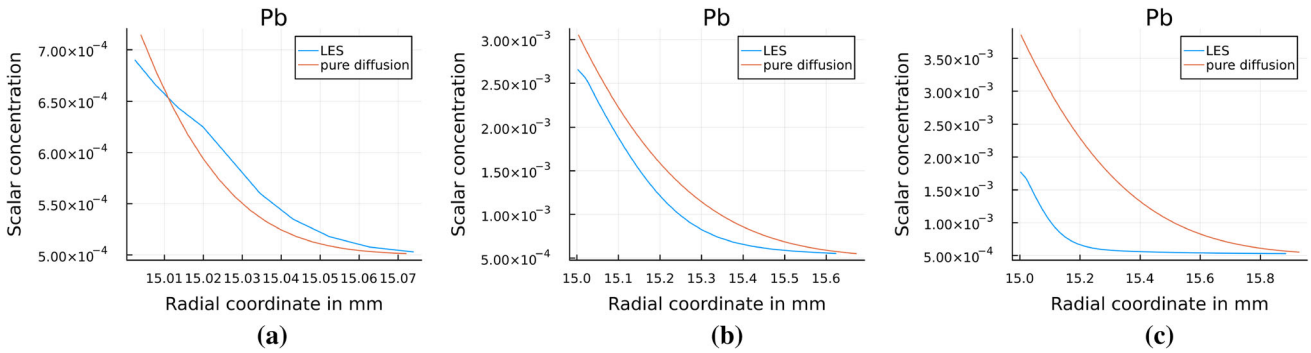

Fig. 17—UDS distribution of Pb: 0.1 s after the beginning of the addition (*a*), 14.4 s after the addition start at the end of the rotation with 25 RPM (switching to 55 RPM) (*b*), 25.0 s after the addition start and a rotation of 55 RPM (*c*).

Fe where refinement is not so enhanced by the increase of the rotation rate.

IV. DISCUSSION

The experimental results applied to the BPS model showed an abrupt decrease in the calculated thickness of the diffusion layer when the rotation increased from 25 to 55 RPM. This increase in rotation resulted in a decrease in the thickness of the diffusion layer, represented as a function of the liquid diffusion coefficient of the investigated impurity in aluminum, of 65 pct for Pb, 88 pct for Si, and 78 pct for Fe.

When the effective distribution coefficient is calculated through the BPS model using the obtained diffusion coefficient, it is possible to clearly observe that the rotation rate has a decreasing effect on the effective distribution coefficient. This translates into a more efficient segregation of impurities, which is supported by the experimental results that show a higher purification at higher rotation rates.

From the results of the phase field simulations, a high sensitivity to the purification effect by parameters such as the temperature gradient or the growth rate can be observed. The sensitivity of the process to these parameters is supported by the experimental observation that an optimal purification effect can be achieved only very

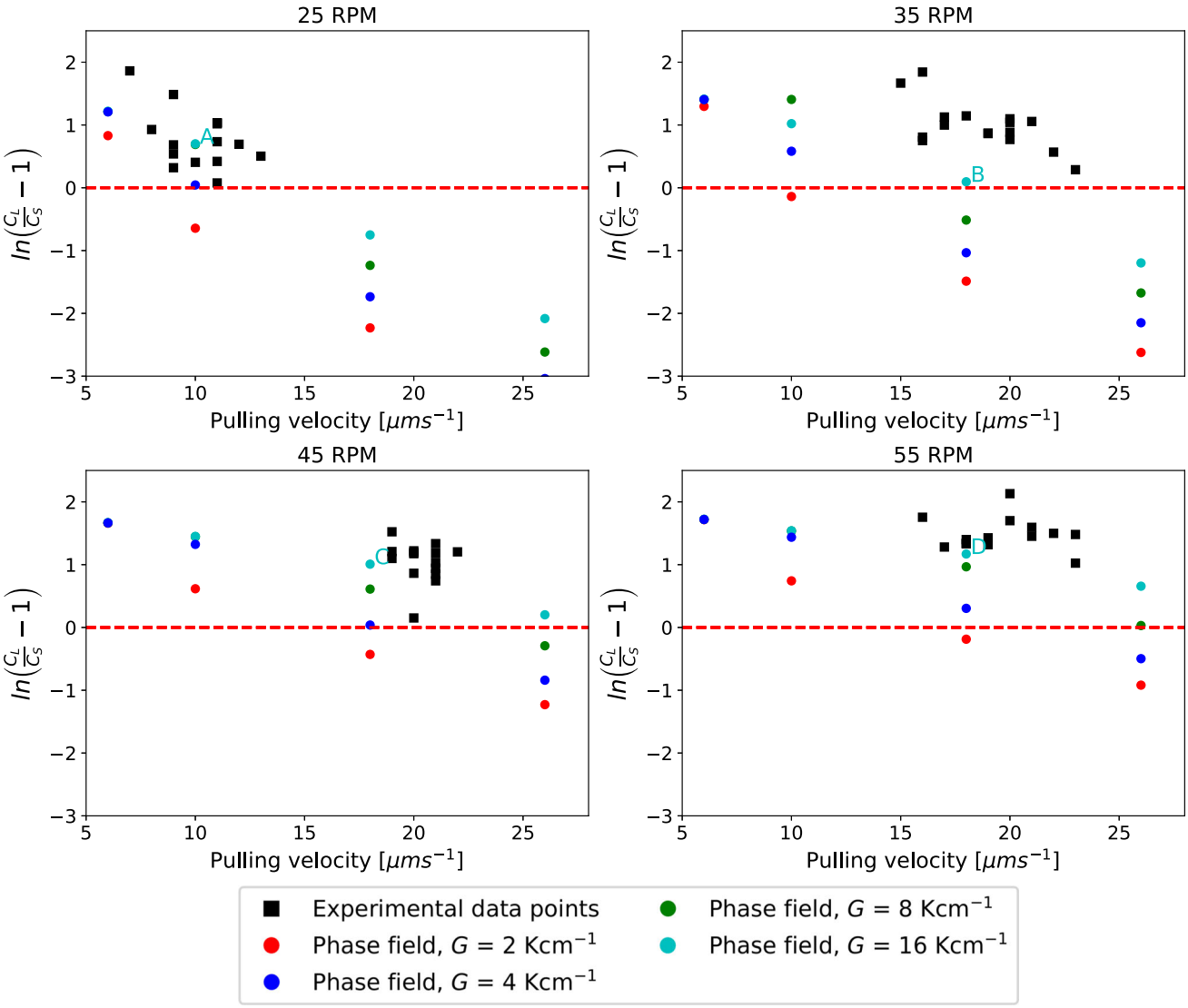

Fig. 18—BPS analysis showing the linear fitting of the obtained growth and $k_{\text{eff}}\frac{C_S}{C_L}$ experimental data (black squares) and phase field simulations (colored dots) for the removal of Pb. Each graph represents the trials conducted at different rotation rates. The dashed red line represents a reduction of impurities of 50 pct (Color figure online).

rarely. On the other hand, there is evidence from the macroscopic CFD simulation results, that no local temperature gradients of the required magnitude can be achieved. However, these results are again strongly dependent on the boundary condition of the wall temperature of the mold. Already 1 to 2 K higher boundary values could lead to a significantly higher agreement. An extension of the computational domain for the simulation of this boundary temperatures based on the furnace's parameters, is probably not useful due to the required accuracy/sensitivity of the temperature determination at this point. The reliability and local accuracy of this boundary condition could be improved on the one hand using several and high-quality (up to now type K—class 2) thermocouples. On the other hand, the calibration to the melting temperature should be checked, as the momentarily correction lies above the accuracy classification of the thermocouple types (more than 10 °C in some cases).

Furthermore, from the scattering of the experimental results regarding the influence of solidification growth rates (Figure 5) as well as the influence of the cooling rate and the rotation rate on the achieved purification effect (Figure 18), it can be seen that the measurements of these variables are subject to higher errors. On the one hand, these are caused by the limitation of the sample quantity due to high analysis costs. On the other hand, they are because no online measurement of the mass solidified on the cylinder or the torque is done. Therefore, at the moment, crystallization time and solidification speed can only be determined as an average over time with relatively low accuracy.

Nevertheless, also in this case, an improvement of the experimental methodology would be necessary, to obtain appropriate evidence.

A transient and optimized recording of inscribed quantities, together with a more homogeneous radial growth of the solidification front (already actively in

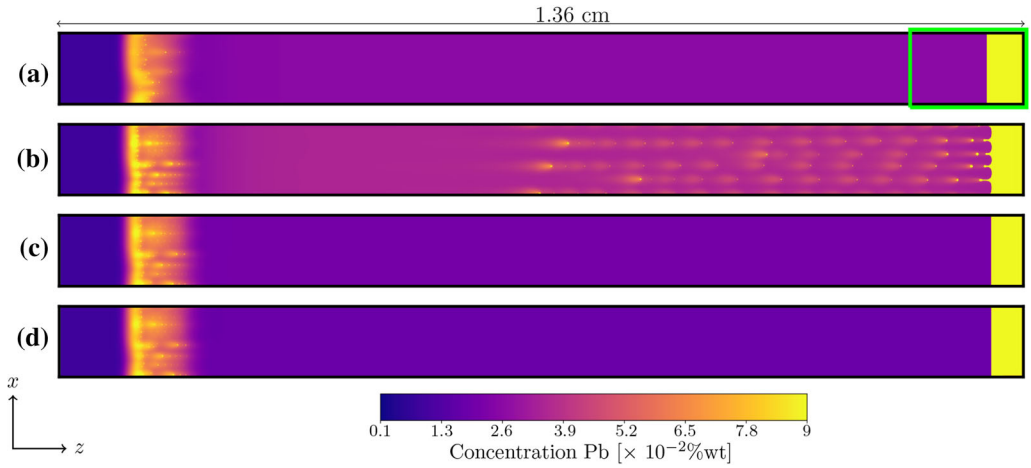

Fig. 19—Spatio-temporal plot of the Pb-concentration field for case (*A*) 25 RPM, $G = 16\ \mu m\ s^{-1}$, $V_{pull} = 10\ \mu m\ s^{-1}$, (*B*) 35 RPM, $G = 16\ \mu m\ s^{-1}$ and $V_{pull} = 18\ \mu m\ s^{-1}$, (*C*) 45 RPM, $G = 16\ \mu m\ s^{-1}$ and $V_{pull} = 18\ \mu m\ s^{-1}$ and (*D*) 55 RPM, $G = 16\ \mu m\ s^{-1}$ and $V_{pull} = 18\ \mu m\ s^{-1}$. The green rectangle represents the size of the moving calculation. The simulated time is 1200 s for case A and 670 s for cases B,C,D (Color figure online).

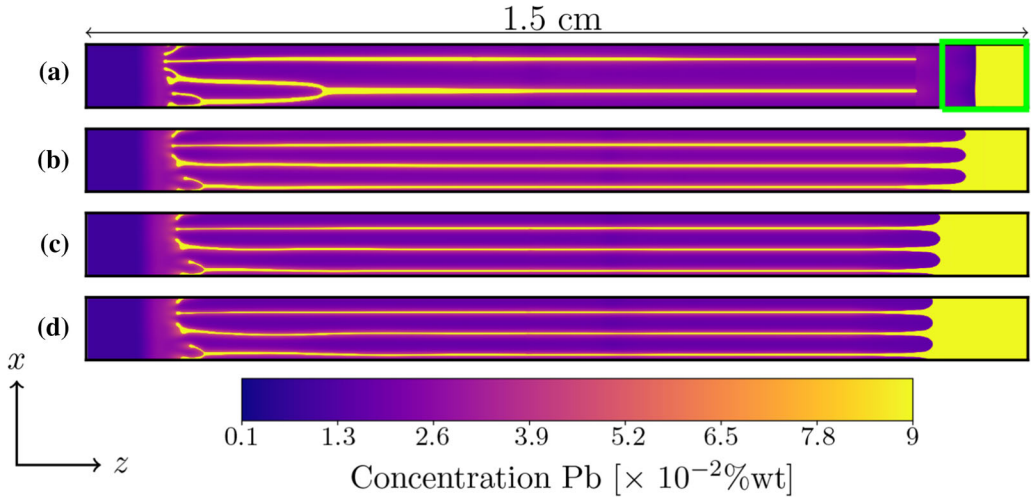

Fig. 20—Spatio-temporal plot of the Pb-concentration field for case (*A*) 25 RPM, $G = 2\ K\ cm^{-1}$, $V_{pull} = 10\ \mu m\ s^{-1}$, (*B*) 35 RPM, $G = 2\ K\ cm^{-1}$ and $V_{pull} = 18\ \mu m\ s^{-1}$, (*C*) 45 RPM, $G = 2\ K\ cm^{-1}$, and $V_{pull} = 18\ \mu m\ s^{-1}$ and (*D*) 55 RPM, $G = 2\ K\ cm^{-1}$ and $V_{pull} = 18\ \mu m\ s^{-1}$. The green rectangle represents the size of the moving calculation. The simulated time is 1200 s for case A and 670 s for cases B, C, D (Color figure online).

progress), is necessary in the future, so that the mechanisms of action of the purification and therefore the optimal process parameters can be better substantiated.

Optimization of the temperature gradient could be forced, for example, by increasing both cooling and heating power. However, this would be accompanied by a reduction of the energy efficiency of the process. Therefore, it could be considered to scale up the process, whereby a stronger scaling in axial direction could additionally force the formation of Taylor vortex structures, which then could additionally be reinforced by a counter rotation of the crucible. Through the formation of these flow structures, it would be conceivable to further increase the local gradient near the solidification front.

Due to the high sensitivity of the process in a very small region near the solidification front, it would be difficult to generate a very reliable macroscopic solidification model. Such a model must cover the entire transient process with mesh sizes around 1 mm to 2 mm, to guarantee reasonable computation times. Here, it would be necessary to close the gap between micro and macro flow structures by validating or modifying different turbulence models and wall law modifications, against a subset of the geometric surface variations within this process. These "closure models" (diffusion layer thickness, local temperature gradient) are normally derived from DNS models or extensive experimental investigations. However, these are overly ambitious goals that are usually only achieved if there is a prominent level of interest in the respective flow form(s).

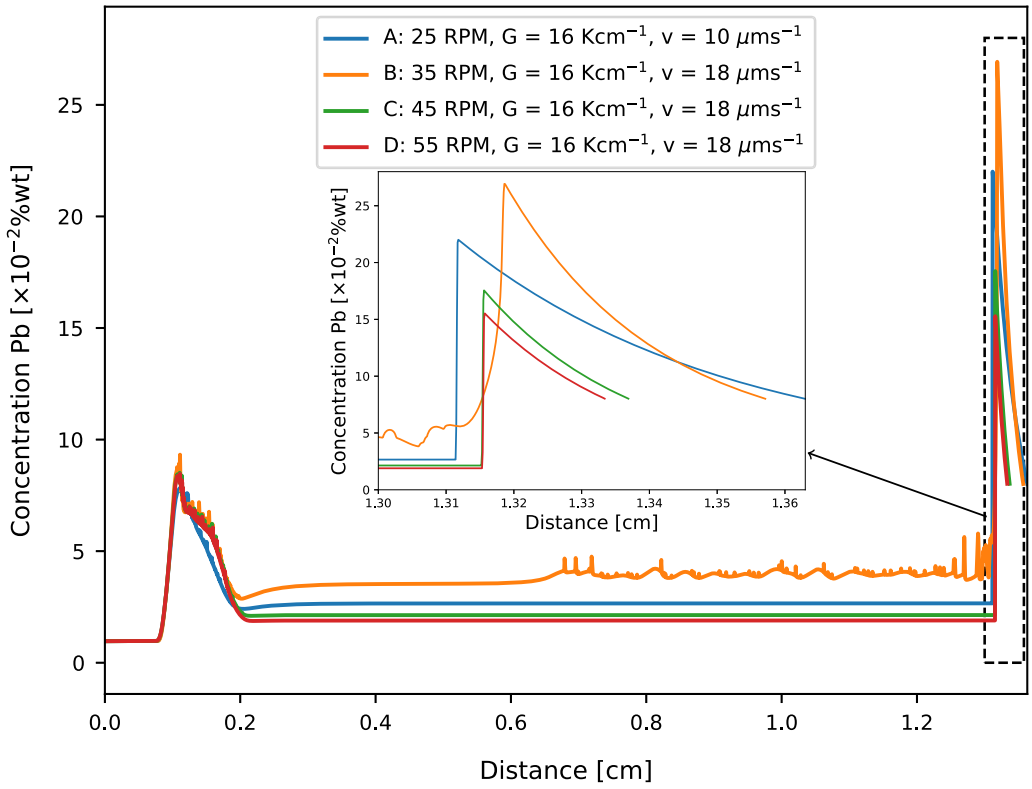

Fig. 21—Pb-concentration profiles as a function of z for case (A), (B), (C), and (D) from Fig. 19, z = 0 corresponds to the bottom of the simulation domain, on the onset: zoom at the pile-up zone defined by the black-dashed box. The simulated time is 1200 s for case A and 670 s for cases B, C, D.

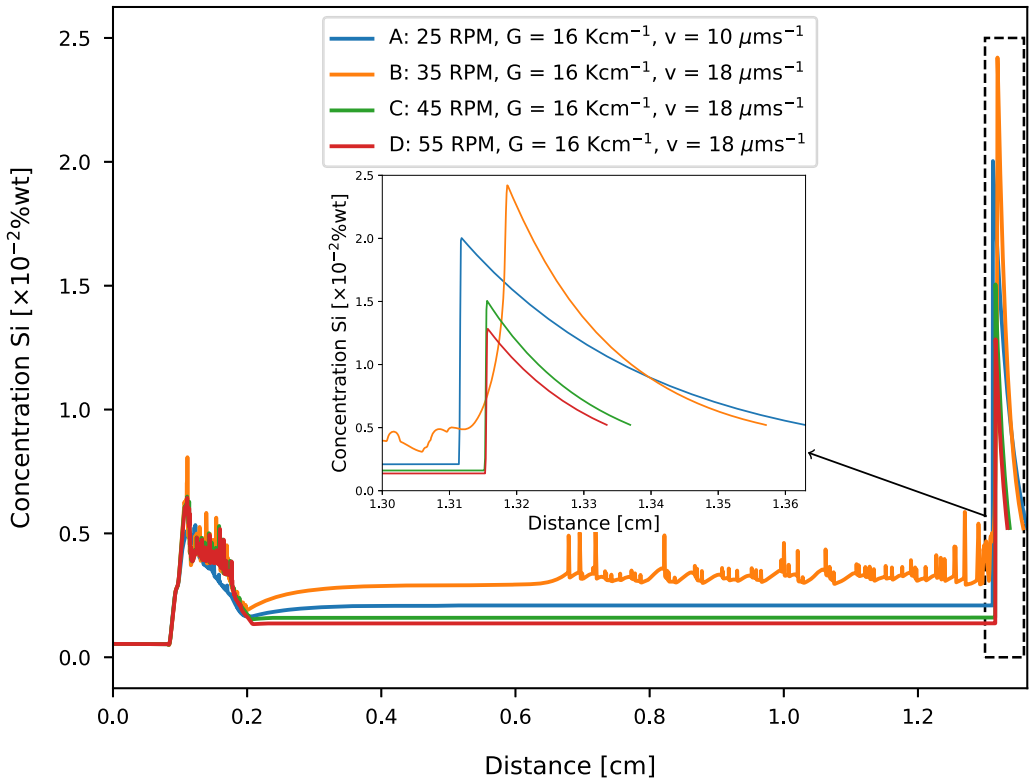

Fig. 22—Si-concentration profiles as a function of z for case (A), (B), (C), and (D) from Fig. 19 , z = 0 corresponds to the bottom of the simulation domain, on the onset: zoom at the pile-up zone defined by the black-dashed box. The simulated time is 1200 s for case A and 670 s for cases B, C, D.

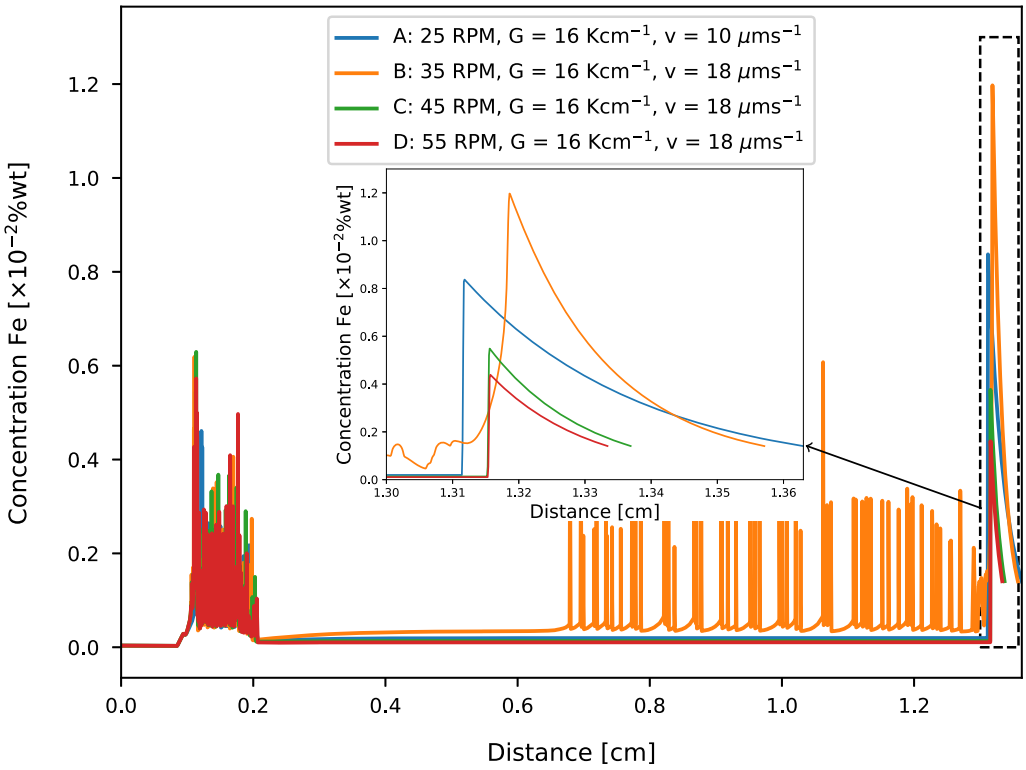

Fig. 23—Fe-concentration profiles as a function of z for case (A), (B), (C), and (D) from Fig. 19 , z = 0 corresponds to the bottom of the simulation domain, on the onset: zoom at the pile-up zone defined by the black-dashed box. The simulated time is 1200 s for case A and 670 s for cases B, C, D.

V. CONCLUSION

The effect of rotation is one of the disruptive characteristics of the cooled finger when compared with another fractional crystallization processes. This characteristic can be attributed mostly due to its design, which favors a very intense convection direct at the solid growth interface. This ultimately leads to much higher solute segregation, and consequently, a high product purification. It has been shown that significant and energy-efficient purification of aluminum from suitable impurity elements can be achieved using the cooled finger methodology.

It has now been possible to identify a stable planar growth front through phase field simulations. According to the phase field results and solidification theory, planar growth front requires elevated temperature gradients (10 to 20 K cm^{-1}) and low solidification velocity (10 to 20 ms). Although both conditions provide stability, they are inefficient in terms of energy consumption and processing time. Phase-field-assisted process simulations could be used to propose energy and time-dependent adjustments to heating and cooling power on the outer edge of the crucible and cooled finger. As part of the design of efficient-processing schemes, it is essential to consider the composition of multicomponent alloys. A time-dependent process control is proposed to prevent cellular growth patterns at the initial stages of the process, achieving stable growth even in transient conditions.

ACKNOWLEDGMENTS

This research funded by the Deutsche Forschungsgemeinschaft (DFG, German Research Foundation)—PF 394/28-1, FR 1713/43-1, and AP 196/20-1.

AUTHOR CONTRIBUTIONS

DCC: Conceptualization, methodology, validation, formal analysis, investigation, writing—original draft/review and editing, visualization, funding acquisition. CS: Conceptualization, methodology, validation, formal analysis, investigation, writing—original draft/review and editing, visualization, funding acquisition. AV: Conceptualization, methodology, validation, formal analysis, investigation, writing—original draft/review and editing, visualization. SF: Conceptualization, writing—review and editing, project administration, funding acquisition. ME: Conceptualization, writing—review and editing, project administration, funding acquisition. BB: Writing—review and editing, methodology. BF: Resources, supervision, funding acquisition. HP: Resources, supervision, funding acquisition. MA: Resources, supervision, funding acquisition.

FUNDING

Open Access funding enabled and organized by Projekt DEAL.

CONFLICT OF INTEREST

The authors declare no conflict of interest.

OPEN ACCESS

APPENDIX A

See Figures 24, 25, 26, 27, and 28.

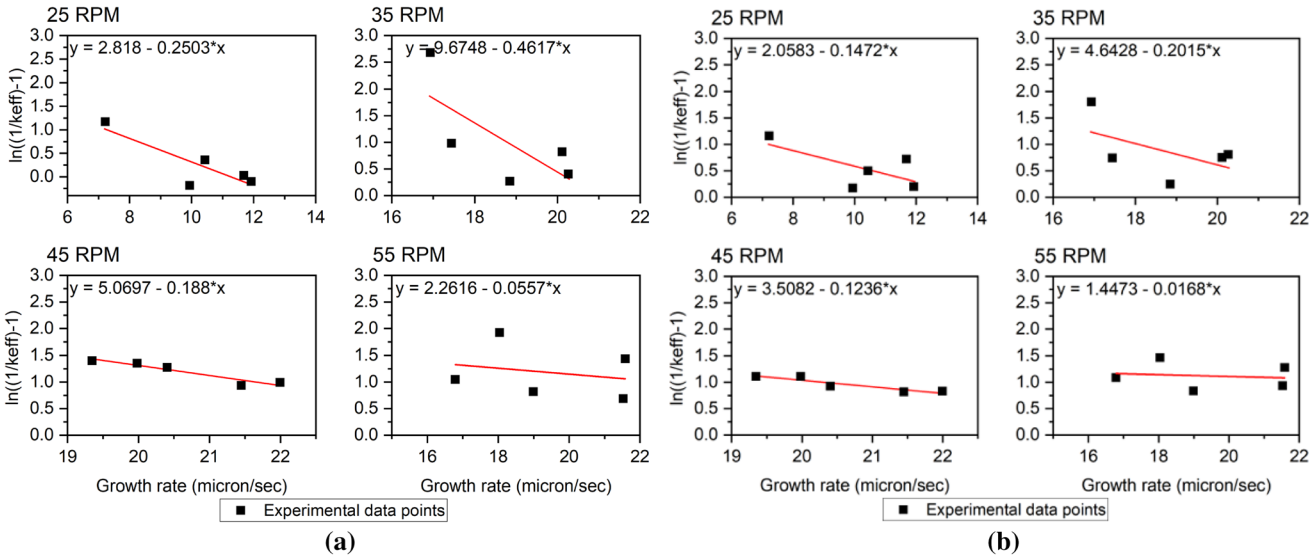

Fig. 24—BPS analysis showing the linear fitting of the obtained growth and k_{eff} experimental data for the removal of Fe (*a*) and Si (*b*). Each graph represents the trials conducted at different rotation rates.

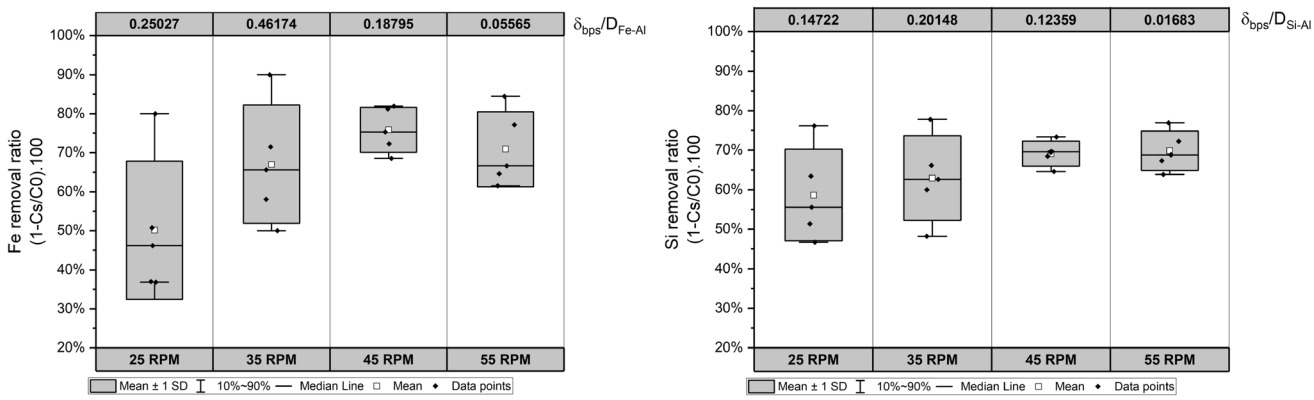

Fig. 25—Influence of the diffusion layer thickness on the obtained Fe (*a*) and Si (*b*) removal ratio from aluminum.

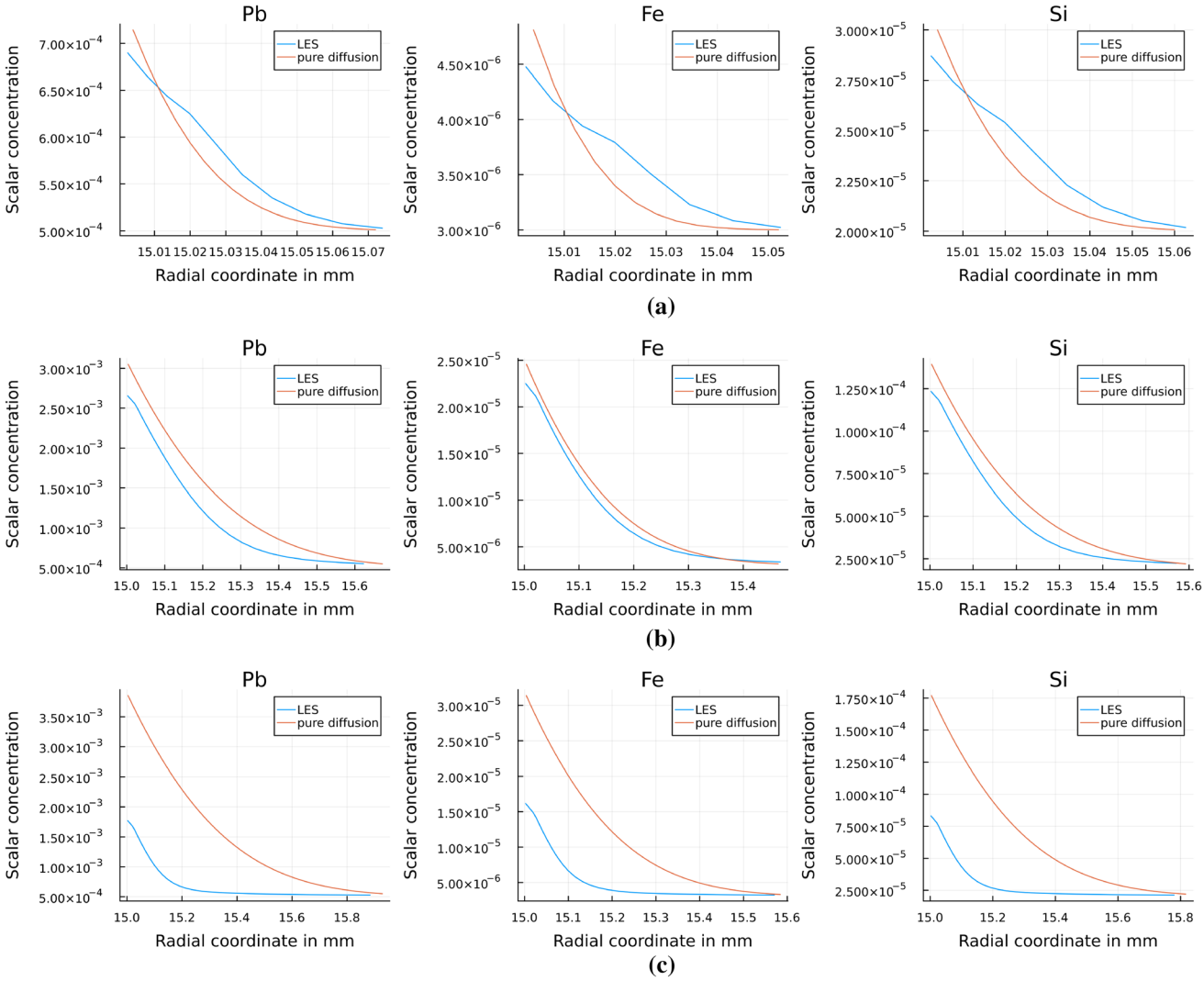

Fig. 26—UDS distribution of different scalar elements: 0.1 s after the beginning of the addition (*a*), 14.4 s after the addition at the end of the rotation with 25 RPM (*b*), 25.0 s after the addition and a rotation of 55 RPM (*c*).

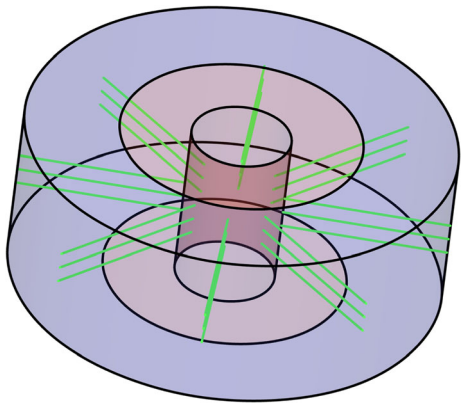

Fig. 27—The 24 lines for the averaging of the UDS values.

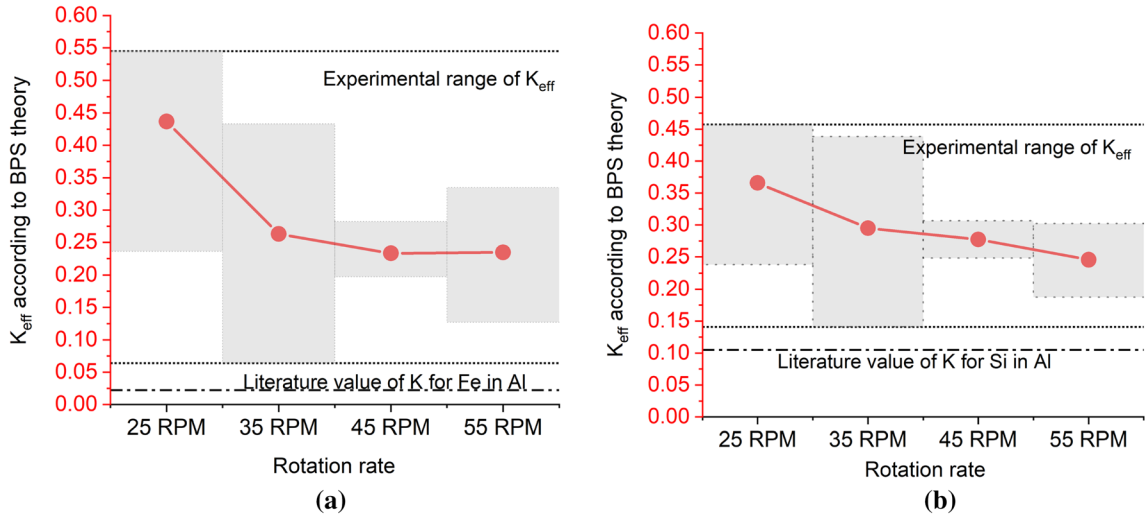

Fig. 28—Effective distribution coefficient of Fe (*a*) and Si (*b*), according to BPS theory, as a function of rotation rate.

REFERENCES

1. M. Leroy: *Le J. Phys. IV*, 1995, vol. 05(C7), pp. C7-99–C7-110. https://doi.org/10.1051/jp4:1995708.
2. H. Zhao and H. Lu: in *Light Metals; Proceedings of the Technical Sessions Presented by the TMS Aluminum Committee at the TMS 2008 Annual Meeting & Exhibition*, Minerals, Metals and Materials Society, Warrendale, 2009, New Orleans, Louisiana, 2008, pp. 533–540.
3. M. Kondo, H. Maeda, and M. Mizuguchi: *JOM*, 1990, vol. 42(11), pp. 36–37. https://doi.org/10.1007/BF03220434.
4. E. Hashimoto, Y. Ueda, and T. Kino: *Le J. Phys. IV*, 1995, vol. 05(C7), pp. C7-153–57. https://doi.org/10.1051/jp4:1995715.
5. H. Hoshikawa, I. Tanaka, and T. Megumi: Refining technology and low temperature properties for high purity aluminum, Sumitomo Kagaku, 2013, pp. 1–12.
6. W.G. Pfann: *Science*, 1962, vol. 135(3509), pp. 1101–09. https://doi.org/10.1126/science.135.3509.1101.
7. S. Mikubo, in *12th International Conference on Proceedings of the 12th International Conference on AluminiumAlloys*, 2010, pp. 224–28.
8. J. A. Burton, R. C. Prim, W. P. Slichter: *J. Chem. Phys.*, 1953, vol. 21, p. 1987. https://doi.org/10.1063/1.1698728.
9. J.V. Widiatmo, K. Harada, K. Yamazawa, and M. Arai: *Metrologia*, 2006, vol. 43(6), pp. 561–72. https://doi.org/10.1088/0026-1394/43/6/012.
10. W.D. Hannibal, G. Ibe, K. Kurre, and H. Peychal-Heiling: Entwicklung eines technischen Verfahrens zur Herstellung von Reinstaluminium für die Kyroelektrotechnik, speziell für Kyromagnete. Tech. Rep., Zentralstelle für Luft- u. Raumfahrtdokumentation u. -information, Munich, Germany, 1974.
11. J. Barthel, E. Buhirg, and E. Al: *Kristallisation aus Schmelzen*, Verlag für Grundstoffindustrie Leipzig, Leipzig, 1982.
12. J.V. Pearce: *Int. J. Thermophys.*, 2014, vol. 35(3-4), pp. 628–35. https://doi.org/10.1007/s10765-014-1585-5.
13. W.H. Sillekens and D. Verdoes: *Metall-Forschung*, 2002, vol. 56(7–8), pp. 468–73.
14. W. Kurz and D.J. Fisher: *Fundamentals of Solidification*, 3rd ed., Trans Tech Publications, Aedermannsdorf, 1989.
15. K.A. Jackson: *J. Cryst. Growth*, 2004, vol. 264(4), pp. 519–29. https://doi.org/10.1016/j.jcrysgro.2003.12.074.
16. W.G. Pfann: *Zone Melting*, Wiley Series on the Science and Technology of Materials, Wiley/Chapman & Hall, New York/London, 1958.
17. M. Chatelain, M. Albaric, D. Pelletier, and V. Botton: *J. Cryst. Growth*, 2015, vol. 430, pp. 138–47. publisher: Elsevier. https://doi.org/10.1016/j.jcrysgro.2015.08.013.
18. J.A. Burton, R.C. Prim, and W.P. Slichter: *J. Chem. Phys.*, 1953, vol. 21(11), pp. 1991–96. https://doi.org/10.1063/1.1698729.
19. A.G. Ostrogorsky and M.E. Glicksman: in *Handbook of Crystal Growth: Bulk Crystal Growth*, 2nd ed, vol. 2, Elsevier, 2014, pp. 1000–18. https://doi.org/10.1016/B978-0-444-63303-3.00025-0.
20. H. Herwig: *Turbulente Strömungen: Einführung in die Physik eines Jahrhundertproblems, Essentials*, Springer Vieweg, Wiesbaden, 2017.
21. H. Herwig: *Strömungsmechanik: Eine Einführung in die Physik und die mathematische Modellierung von Strömungen*, Springer Berlin, 2007. https://books.google.de/books?id=-fcmBAAAQBAJ.
22. J. Bredber: On the Wall Boundary Condition for Turbulence Models, Internal Report 00/4, 2000.
23. D. Curtolo, S. Friedrich, D. Bellin, G. Nayak, and B. Friedrich: *Metals*, 2017, vol. 7(9), p. 341. https://doi.org/10.3390/met7090341.
24. P.R.N. Childs: *Rotating Flow*, Elsevier, Amsterdam, 2011.
25. Y.-J. Kim and Y.-K. Hwang: *KSME Int. J.*, 2003, vol. 17(4), pp. 562–70. https://doi.org/10.1007/BF02984457.
26. R. Ostilla-Mónico, E.P. van der Poel, R. Verzicco, S. Grossmann, and D. Lohse: *Phys. Fluids*, 2014, vol. 26(1), p. 015114. https://doi.org/10.1063/1.4863312.
27. I. Ansys: ANSYS Academic Research, Release 2022 R1 Help System, FLUENT Theory Guide 2022, 2022.
28. F.R. Menter: *Best Practice: Scale-Resolving Simulations in ANSYS CFD*, Ansys Germany GmbH, Darmstadt, 2015.
29. A. Viardin, B. Böttger, and M. Apel: *Mater. Theory*, 2022, vol. 6(1) pp. 1–22. https://doi.org/10.1186/s41313-022-00042-y.
30. MICRESS 7.1: http://www.micress.de.
31. J. Eiken, B. Böttger, and I. Steinbach: *Phys. Rev. E*, 2006, vol. 73(6), p. 66122.
32. B. Böttger, J. Eiken, and M. Apel: *Comput. Mater. Sci.*, 2015, vol. 108, pp. 283–92. https://doi.org/10.1016/j.commatsci.2015.03.003.
33. Thermo-Calc database TCAL6: https://www.thermocalc.com/, accessed 1 July 2021.
34. B. Böttger, J. Eiken, and M. Apel: *J. Comput. Phys.*, 2009, vol. 228(18), pp. 6784–95. https://doi.org/10.1016/j.jcp.2009.06.028.
35. M. Leitner, T. Leitner, A. Schmon, K. Aziz, and G. Pottlacher: *Metall. Mater. Trans. A*, 2017, vol. 48A(6), pp. 3036–45. https://doi.org/10.1007/s11661-017-4053-6.
36. M.J. Assael, K. Kakosimos, and R.M. Banish: *J. Phys. Chem. Ref. Data*, 2006, vol. 35(285), p. 17. https://doi.org/10.1063/1.2149380.
37. W. Sun, L. Zhang, M. Wei, Y. Du, and B. Huang: *Trans. Nonferrous Met. Soc. China*, 2013, vol. 23(12), pp. 3722–28. https://doi.org/10.1016/S1003-6326(13)62922-2.